JRC Scientific and Technical Reports

Calibration and Modeling of PMP compliant Condensation Particle Counters

Athanasios Mamakos, Barouch Giechaskiel*, Yannis Drossinos, Dominique Lesueur, Giorgio Martini, Alois Krasenbrink

Present address: AVL List GmbH, Hans-List-Platz 1, A-8020 Graz, Austria

EUR 25145 EN - 2011

JRC EUROPEAN COMMISSION

Institute for Energy and Transport

EMRP
European Metrology Research Programme
Programme of EURAMET

The EMRP is jointly funded by the EMRP participating countries within EURAMET and the European Union

The mission of the Joint Research Centre – Institute for Energy and Transport (IET) is to provide support to Community policies and technology innovations related both:

- to energy, to ensure sustainable, safe and efficient energy production, distribution and use and
- to transport, to foster sustainable and efficient mobility in Europe.

European Commission
Joint Research Centre
Institute for Energy and Transport

Contact information
Giorgio Martini
Address: Via E. Fermi 2749, I-21027, Ispra (VA), Italy
E-mail: giorgio.martini@jrc.ec.europa.eu
Tel.: +39 0332 789293

http://iet.jrc.ec.europa.eu/
http://www.jrc.ec.europa.eu/

JRC 67661

EUR 25145 EN
ISBN 978-92-79-22610-6 (pdf)
ISBN 978-92-79-22609-0 (print)
ISSN 1831-9424 (online)
ISSN 1018-5593 (print)
doi:10.2788/41597

Luxembourg: Publications Office of the European Union, 2011

Printed in Italy

TABLE OF CONTENTS

ACKNOWLEDGMENTS 6

1 INTRODUCTION 7

2 EXPERIMENTAL 9

2.1 Aerosol Instrumentation 9

2.2 Aerosol Generators 9

2.3 Calibration Setup 10

2.3.1 Calibration of the DMAs 10

2.3.2 Calibration of the 3025A CPC 10

2.3.3 Calibration of the “Golden” 3790 CPC against the electrometer 11

2.3.4 Calibration of the 3790 and 3010 CPCs against the 3025A CPC 12

3 THEORETICAL CONSIDERATIONS 14

3.1 CPC detection efficiencies 14

3.1.1 Basic model 14

3.1.2 Additional investigations on the 3790 detection efficiencies 20

3.2 Simulated Tandem DMA responses 32

4 RESULTS 37

4.1 DMA Calibration 37

4.2 Calibration of the 3025A CPC 39

4.3 Linearity measurements 41

4.3.1 Sample pressure effect 41

4.3.2 CPC spikes occurring during butanol filling 42

4.3.3 Linearity tests 43

4.4 Detection efficiencies 46

4.4.1 Pressure effect 46

4.4.2 CPC inter-comparisons 47

4.4.3 Counting efficiencies of the 3790_Gold CPC 48

4.4.4 Counting efficiencies of the 3790_JRC CPC 50

4.4.5 Effect of the operating temperatures on the peak detection efficiencies of the 3790 CPC 52

4.4.6 Counting efficiencies of the 3010 CPC.....53

4.4.7 Counting efficiencies for C14,C16 and C40 55

4.4.8 Effect of particle charge state.....56

5 CONCLUSIONS.....58

6 LIST OF SPECIAL TERMS AND ABBREVIATIONS.....60

REFERENCES 61

ACKNOWLEDGMENTS

The authors would also like to gratefully acknowledge Carsten Gruening and Sebastiao Martin Dos Santos for providing the nebulizer used for the calibration of the DMAs. We would also like to thank INEOS Oligomers for supplying us with Poly-(alpha) Olefin employed in the calibration experiments.

The authors would also like to acknowledge TSI for providing the Golden CPC employed in the calibration experiments.

The present study was partially funded by the EMRP-ENV02 PartEmission project. The EMRP is jointly funded by the EMRP participating countries within EURAMET and the European Union.

1 INTRODUCTION

Starting from September 2011, all new type approved diesel passenger cars in Europe will have to comply with a particle number limit of 6×10^{11} #/km measured in accordance with the Particle Measurement Programme (PMP) procedures [1, 2]. The regulation requires sampling from a Constant Volume Sampler (CVS) using a measurement system that dilutes and thermally treats the extracted sample to remove volatile material. The concentration of the conditioned aerosol is then measured with a full flow Condensation Particle Counter (CPC) having a nominal 50% detection efficiency at 23 nm electrical mobility diameter. A similar requirement will be introduced shortly for the certification of Heavy Duty Engines (HDE) [3].

The regulation includes some specifications for the CPCs, the main being:

- Operation in full flow mode (i.e. internal splitting of the flows is prohibited).
- Linear response to particle concentrations over the full measurement range in single particle count mode (typically up to 10000 #/cm^3).
- Counting accuracy of ±10% across the range from 1#/cm^3 to the upper threshold of the single particle count mode against a traceable standard.
- 50%±12% and >90% counting efficiencies at electrical mobility diameters of 23 ±1 nm and 41 ±1 nm, respectively.

The regulation also specifies an annual calibarion requirement which should be performed either against an electrometer (primary method) or against a CPC (secondary method) which has been directly calibrated by the primary method. The CPC under calibration shall sample simultaneously with the reference instrument electrostatically classified calibration particles.

The regulation does not specify the calibration material type that should be employed in the calibrations. Yet a number of studies have identified a strong material dependence for all commercial CPC systems complying with the European regulation requirements [4, 5]. Numerical computations [6] provided evidence that the strong material dependence observed in the experimentally determined counting efficiencies is to a large extent related to the low saturation ratios employed in these CPCs (required to achieve 50% counting efficiency at a relatively large size of 23 nm). However, some systematic discrepancies were observed between the numerical model and experimental results with emery oil and tetracontane, which were attributed to contamination of the calibration particles.

One additional challenge in the calibration of CPCs relates to the low sensitivity of the electrometers [7]. Calibration certificates supplied by the CPC manufacturers typically cover the 2000 to 10000 #/cm^3 concentration range. Yet, the concentrations measured during type-approval tests can be well below 100 #/cm^3.

The purpose of the present study is twofold:

a) to investigate possibilities to increase the sensitivity of the electrometer allowing calibration of CPCs at concentration levels below 2000 #/cm^3 and

b) to provide some more insights on the dependence of the CPC counting efficiencies on the material type.

Two approaches were considered for the calibration of CPCs at low particle concentrations. The first one included the operation of the electrometer at higher sample flowrates. The second one included the use of multiply charged particles of a well defined charged state using a Tandem Differential Mobility Analyzer (TDMA) system.

The majority of the calibration experiments were performed on a CPC that was subsequently circulated in an interlaboratory correlation exercise conducted in the framework of the PMP project (PMP VPR Round Robin). The particular interlaboratory correlation activity, that is currently underway, aims at the assessment of the comparability of the calibration procedures employed by different manufacturers and research institutions in characterizing particle number measurement systems.

2 EXPERIMENTAL

2.1 Aerosol Instrumentation

The study mainly focused on the performance of the TSI 3790 Condensation Particle Counter (CPC) that was circulated as a “Golden” instrument in the PMP VPR Round Robin. Some experiments were also performed with two other CPCs of the same model (referred to as 3790_JRC, 3790_APC in the document to discriminate them from the golden 3790_Gold) and a TSI 3010 CPC.

A TSI 3068B electrometer and a TSI 3025A CPC were employed as the reference instruments against which the 3790 and 3010 CPCs were calibrated. The 3025A CPC was shipped for maintenance at TSI 6 months before the measurement campaign and was also checked against the 3068B electrometer before the tests. The 3010 indications were corrected for coincidence using the empirical formula suggested by the manufacturer [8].

Three in total Differential Mobility Analyzers (DMAs) were employed in the measurement campaign. These included a TSI 3085 Nano DMA (Nano-DMA), a TSI 3081 Long DMA (LDMA), and a Grimm 5.5-900 DMA (Grimm-DMA). The Nano-DMA was employed for the calibration of the reference 3025A CPC while the two other DMAs were employed in a tandem setup to calibrate the 3790 and 3010 CPCs (see sections 2.3.3 and 2.3.4). The LDMA and the Nano-DMAs were regularly connected in a TSI 3936 Scanning Mobility Particle Sizer (SMPS) to measure the number-weighted mobility size distributions. The operating flowrates of the DMAs were checked on a regular basis against a bubble flowmeter (Gillian Gilibrator 2).

2.2 Aerosol Generators

The calibration aerosols employed in the study included graphite, Poly(alpha)-Olefin (PAO), tetracontane (C40), tetradecane (C14), hexadecane (C16), silver and PolyStyrene Latex (PSL) particles. The 3790 and 3010 CPC calibrations were mainly performed using graphite and PAO particles. However, the counting efficiencies of the 3790_JRC CPC were also experimentally determined for C40, C16 and C14. The silver particles were employed for the calibration of the 3025A CPC, while the PSL spheres were used for the calibration of the LDMA and the Grimm-DMA.

Graphite particles were produced by spark discharge (DNP3000 from PALAS GmbH), while PAO, C40, C14 and C16 particles were generated by evaporation-condensation (JRC home made generator – [9]). Silver particles were produced in a home-made, Silver Particle Generator (SPG) which was based on the design described by Gotoh et al. [10] (the actual implementation of which is described in more details in [9]). PSL particles having a NIST traceable size of 498±5 nm mobility diameter (Thermo Scientific 3500A) were resuspended in an ultrasonic nebulizer (CETAC U5000AT+). The suspensions of the polystyrene particles were prepared by diluting 1 drop of the original water suspensions (1% concentration) with 10 ml of ultrapure water (milli-Q quality). Purified shop-air (HEPA filtered, dehumidified) and/or bottled nitrogen were employed in all generators to minimize contamination of the generated particles from impurities in the gases [4].

The evaporation-condensation generator was thoroughly cleaned between changes of the working liquid (PAO, C14 and C16), by means of extended operation at elevated temperatures and through use of nitrogen flow to purge the vapours remaining after removing the liquid from the evaporator compartment. Following the tests with tetracontane, however,

deposits of paraffin-like wax were observed on all walls of the generator that could not be removed effectively with the aforementioned procedure. The limited number of tests performed following the tetracontane experiments, suggested contamination of the generated aerosol and were therefore disregarded from any subsequent analysis.

2.3 Calibration Setup

2.3.1 Calibration of the DMAs

The resuspended polystyrene aerosol exiting the nebulizer first passed through a nafion dryer to ensure that the generated particles contained no moisture. The size distribution of the generated aerosols was first measured with the TSI 3936L10 SMPS to verify that it is possible to discriminate the polystyrene peak from the background concentrations. Comparison checks with and without the nafion dryer showed no differences in the recorded size distributions, suggesting that the aerosol was effectively dried in the nebulizer.

Following these preliminary checks, the calibration aerosol was neutralized and then fed to the DMA under evaluation. A 0.1 mCi ^{241}Am neutralizer (Grimm 5.522) was employed for the calibration of the Grimm-DMA, and a 10 mCi ^{85}Kr neutralizer (manufactured by Eckert and Ziegler GmbH) for the calibration of the LDMA. The DMAs operated at step-wisely increasing and decreasing centre-rod voltages and the concentrations of the classified particles was recorded by a CPC (Grimm's 5403 for the Grimm-DMA, and TSI's 3010 for the LDMA). Both DMAs operated at a sheath flow rate of 3 lpm.

2.3.2 Calibration of the 3025A CPC

Figure 1 illustrates a schematic of the calibration setup employed for the calibration of the 3025A CPC against the electrometer. The silver nanoparticles produced in the SPG first passed through the 10 mCi ^{85}Kr neutralizer where, due to their small size (smaller than 15 nm), practically acquired at maximum a single charge. The charged nanoparticles were subsequently size classified in the Nano-DMA which operated at sheath and sample flowrates of 15 and 1.5 lpm, respectively. The monodisperse particles exiting the Nano-DMA were mixed with purified shop-air that was provided at a flowrate of 1.5 lpm through a mass flow controller. The two streams merged into a single flow in a 0.7 m long conductive silicon tube which was found to allow for a sufficient mixing (as verified by the better than ±2% agreement observed with tests performed using a longer tube (~1.5 m)). The diluted monodisperse flow was subsequently split in two streams in a metallic Y-type connector to allow for the parallel measurement with the 3025A CPC and the 3068 electrometer, both running at a volumetric flowrate of 1.5 lpm. The two instruments were connected to the Y-type connector through conductive silicon tubing of the same length (15 cm) to ensure similar transport losses.

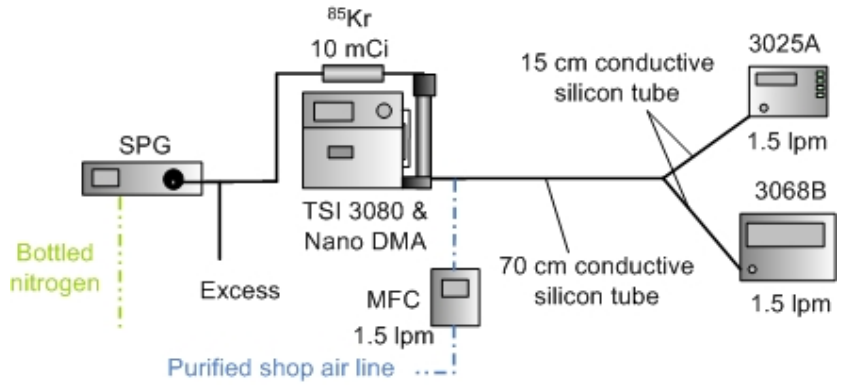

Figure 1: Experimental setup employed for the calibration of the 3025A CPC.

2.3.3 Calibration of the "Golden" 3790 CPC against the electrometer

The linearity of the 3790_Gold CPC was checked against the 3068B electrometer. A schematic of the setup employed in these experiments is illustrated in Figure 2. Graphite aerosol generated in the DNP 3000 was first diluted in a dilution bridge and then passed through a TSI 1035900 impactor (equipped with a 0.071 cm nozzle) to remove particles having an aerodynamic diameter larger than approximately 1 μm. The particles were then size classified in a tandem DMA (TDMA) setup, consisting of the Grimm DMA connected in series with the LDMA. This TDMA configuration effectively minimizes the contribution of larger, multiply-charged particles in DMA-classified aerosols. In these experiments, the Grimm-DMA and the LDMA were equipped with the 0.1 mCi ^{241}Am (Grimm's 5.522) and the 10 mCi 85Kr neutralizers, respectively. The Grimm-DMA operated at a fixed sheath flowrate of 3 lpm, while the sheath flowrate of the LDMA and the sample flowrate of the TDMA were set at 10 lpm and 1 lpm, respectively.

The 3790_Gold CPC was sampling classified graphite particles in parallel with the 3068B electrometer, using two 15 cm long conductive silicon tubes connected in a metallic Y-type connector. A 70 cm long conductive silicon tube served as a mixing chamber to allow sufficient mixing between the aerosol classified in the TDMA and the necessary make-up air. The latter was provided from the laboratory's, conditioned (HEPA filtered, charcoal scrubbed) shop air line through a mass flow controller set at the flowrate of the electrometer. The 3790_Gold CPC operated at its nominal flowrate of 1 lpm, while the 3068B electrometer flowrate was set at either 1 lpm or 5 lpm.

Before starting each test sequence, the 3010 CPC was connected to the LDMA in a 3936L10 SMPS configuration (at the same flow-settings with the TDMA setup) to measure the distribution of particles classified in the Grimm-DMA. A 300 s scan time was employed to minimize the distortion of the DMA transfer function [11] and the dynamics of the CPC response [12].

The electrometer and the 3790 CPC were subsequently connected in the configuration shown in Figure 2. A bubble flowmeter was then used to measure the operating volumetric flowrates of the TDMA system (sample flowrate, sheath flowrates) and the two aerosol detectors (3068B and 3790) with all instruments connected in the calibration configuration. Two types of leakage checks were performed. In the first one, the Grimm-DMA was set at zero voltage with the LDMA scanning the size distribution to verify that the two aerosol detectors were measuring zero. In the second check, the Grimm-DMA was set at a voltage

corresponding to the desired particle size and the LDMA was set at zero voltage to verify again that the two aerosol detectors were measuring zero. During these checks the electrometer was also zeroed if necessary.

Following these checks, the actual CPC calibration tests were performed. The two DMAs were configured to classify particles at the desired mobility diameter and the voltage of the LDMA was sequentially toggled on and off in order to regularly check for zero drifts of the electrometer. Following each voltage change (zero / set point) of the LDMA the instruments were allowed to stabilize at their new concentration levels for at least 30 s and then the concentrations were recorded for 90 s. At the end of each test sequence (i.e. tests at a given particle size or electrometer flowrate setting) the voltage of the two DMAs were set at zero and the operating flowrates of both the DMAs and the aerosol detectors were checked again for drifts using the bubble flowmeter.

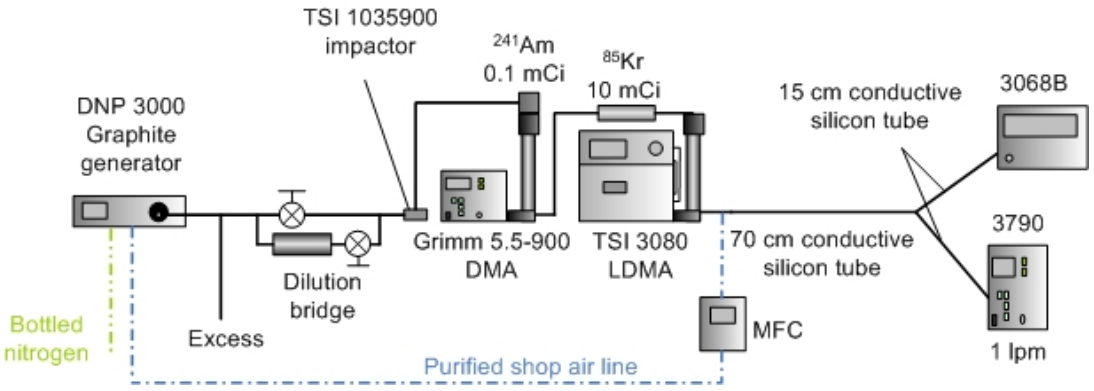

Figure 2: Experimental setup employed for the calibration of the "Golden" 3790 CPC against the electrometer.

2.3.4 Calibration of the 3790 and 3010 CPCs against the 3025A CPC

Figure 3 shows the experimental setup employed for the calibration of the 3790 and 3010 CPCs against the reference 3025A CPC. In principle, the setup was the same to that employed for the calibration of the 3790 Gold CPC against the 3068B electrometer. One notable difference was that a 1 mCi ^{85}Kr neutralizer was employed in some tests to investigate the effect of the particle charging state on the measured detection efficiencies. The two DMAs operated at a sheath flowrate of 3 lpm (Grimm-DMA) and 10 lpm (LDMA) while the sample flowrate was adjusted to 1 lpm. The 3025A CPC operated always at high flow mode (i.e. sample flowrate of 1.5 lpm). To compensate for the different flowrates of the 3025A and the 3790 or 3010 CPCs under calibration, a different length of conductive silicon tubing was employed for the connection of the two CPCs to the Y-type splitter (15 cm for the 3025A and 10 cm for the 3010 or 3790).

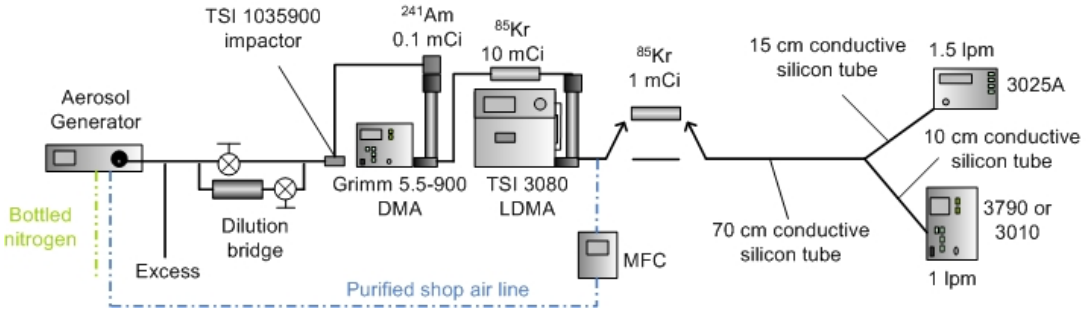

Figure 3: Experimental setup employed for the calibration of the 3790 and 3010 CPCs against the 3025A.

3 THEORETICAL CONSIDERATIONS

3.1 CPC detection efficiencies

In order to better understand the performance of the 3790 CPC, and particularly the effect of particle material type on the experimentally determined detection efficiencies, some numerical calculations were also performed. The basis for these calculations was the heterogeneous nucleation model developed by Giechaskiel et al. [6] (hereinafter referred to as basic model).

Some additional calculations were also performed to investigate the effect of the assumptions made in the basic model. These examined the effect of a) curvature dependence of the surface tension, b) line tension, c) non-idealities in the inlet temperature and velocity profiles, c) particle charge state and d) condensational growth of activated particles.

3.1.1 Basic model

3.1.1.1 Saturation ratio and temperature profiles in the CPC condenser

At a first stage the model calculates the saturation ratio profile inside the condenser by considering a two dimensional heat and mass transfer in forced laminar flow through a circular tube. Under the assumptions of a hydrodynamically fully developed flow (resulting in parabolic Poiseuille velocity profile), constant fluid properties, low vapour concentration and negligible axial diffusion and energy dissipation, the equation describing both mass and heat transfer can be written in dimensionless form as:

$$\left(1-r^2\right)\frac{\partial \vartheta_G}{\partial x} = \frac{\partial^2 \vartheta_G}{\partial r^2} + \frac{1}{r}\frac{\partial \vartheta_G}{\partial r} \qquad \text{eq. 1}$$

where:

$$r = \frac{R}{R_t} \qquad \text{eq. 1a}$$

$$x = \begin{cases} \dfrac{X\alpha}{2R_t^2 U_{ave}}, \text{ for heat transfer} \\ \dfrac{XD_b}{2R_t^2 U_{ave}}, \text{ for mass transfer} \end{cases} \qquad \text{eq. 1b}$$

$$\vartheta_G = \begin{cases} \dfrac{T(r,x)-T_w}{T_{in}-T_w}, & \text{for heat transfer} \\ \dfrac{C_b(r,x)-C_{b,sat}(T_w)}{C_{b,sat}(T_{in})-C_{b,sat}(T_w)}, & \text{for mass transfer} \end{cases} \qquad \text{eq. 1c}$$

with r and x the dimensionless radial and axial coordinates, R_t the tube radius, T_{in} the uniform inlet temperature, T_w the constant wall temperature, C_b the vapour concentration of

butanol, U_{av} the average flow velocity, α the fluid thermal diffusivity and D_v the butanol/air binary diffusion coefficient.

Under the additional assumption that butanol vapour behaves as an ideal gas, the concentration of saturated butanol vapours at the inlet, $C_{b,sat}(T_{in})$, and the condenser walls, $C_{b,sat}(T_w)$, can be written as a function of the butanol saturation vapor pressure, $P_{b,sat}$, butanol molecular weight, M_b, and the universal gas constant, R_g:

$$C_{b,sat}(T_{in}) = \frac{P_{b,sat}(T_{in})M_b}{R_g T_{in}} \qquad \text{eq. 2a}$$

$$C_{b,sat}(T_w) = \frac{P_{b,sat}(T_w)M_b}{R_g T_w} \qquad \text{eq. 2b}$$

The resulting differential equation problem with the corresponding boundary conditions was solved following the numerical method proposed by Housiadas et al. [13]. The calculated butanol vapour concentrations and temperatures (thus saturation butanol vapour concentrations) allowed for the calculation of the saturation ratio, S, profile inside the condenser.

Figure 4 shows the calculated saturation ratio profile inside the 3790 condenser, at the manufacturer set operating temperatures of the 3790_Gold CPC. The peak saturation ratio is approximately 1.22 and occurs close to the inlet and along the tube centerline.

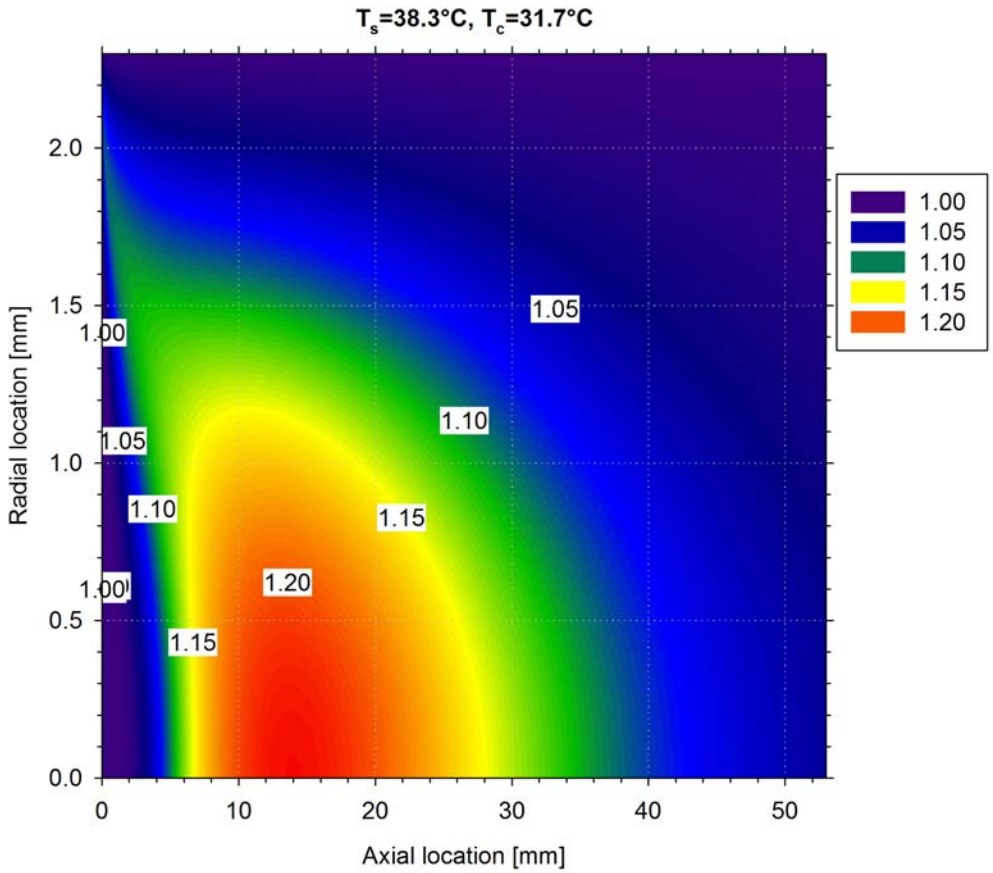

Figure 4: Calculated saturation ratio profile inside the condenser at the nominal operating temperatures of the 3790_Gold CPC.

3.1.1.2 Particle activation

In a second step, the activation probabilities inside the CPC condenser were calculated assuming heterogeneous nucleation of butanol vapours onto the sampled, seed particles [14]. According to heterogeneous nucleation theory (a kinetic process), the probability that a cluster of butanol has adequately large size (critical cluster) to initiate particle growth is:

$$P_{act}(t) = 1 - \exp(-I_{het} t) \qquad \text{eq. 3}$$

where, I_{het} is the activation rate constant per seed particle, or else heterogeneous nucleation rate (nucleated clusters per s), and t is the time the seed particle spends in a zone within the CPC where nucleation may occur. The heterogeneous nucleation rate depends on the properties of the vapour but also on the physicochemical properties of the seed particles, and may be expressed in an Arrhenius form as:

$$I_{het} = I_{het}^{0} \exp\left(-\frac{\Delta G_{het}^{*}}{k_B T}\right) \qquad \text{eq. 4}$$

where k_B is the Boltzman constant, I^0_{het} is a kinetic prefactor and ΔG^*_{het} is the free energy of formation of a critical cluster on the particle surface. Under the assumptions of negligible line tension and size-independent surface tension, σ_{gl}, the free energy of formation of a critical spherical cluster of radius r^* onto a spherical particle of diameter d_p can be expressed as a fraction of the free energy of formation (ΔG^*_{hom}) of a homogeneously nucleated cluster of critical radius r^* [14]:

$$\Delta G_{het}^{*} = f_g \Delta G_{\text{hom}}^{*} \qquad \text{eq. 5}$$

where according to classical nucleation theory:

$$\Delta G_{\text{hom}}^{*} = \frac{4}{3}\pi\left(r^{*}\right)^2 \sigma_{gl} \qquad \text{eq. 5a}$$

$$r^{*} = \frac{2\sigma_{gl} M_b}{\rho_b R_g T \ln S} \qquad \text{eq. 5b}$$

with ρ_b being the density of liquid butanol. Note that the critical radius is half the Kelvin diameter.

The multiplicative factor, f_g, in eq. 5 arises from geometric considerations and takes into account the contact angle, θ, between the critical cluster and the curved surface (thus the particle affinity for butanol):

$$f_g = \frac{1}{2}\left[\begin{array}{l} 1 + \left(\frac{1 - X\cos\theta}{g}\right)^3 + X^3\left(2 - 3\left(\frac{X - \cos\theta}{g}\right) + \left(\frac{X - \cos\theta}{g}\right)^3\right) \\ + 3X^2\cos\theta\left(\frac{X - \cos\theta}{g} - 1\right) \end{array}\right] \qquad \text{eq. 6}$$

with

$$X = \frac{d_p}{2r^*} \qquad \text{eq. 6a}$$

$$g = \sqrt{1 + X^2 - 2X\cos\theta} \qquad \text{eq. 6b}$$

The contact angle takes values from 0 to 180°, and its effect on the heterogeneous nucleation mechanism is illustrated in Figure 5. A contact angle of 180° indicates no affinity of the particle for butanol, in which case the butanol can only be homogeneously nucleated *(f_g* equals 1). At smaller contact angles, the particle can act as a seed onto which the butanol cluster can be developed and this reduces the energy barrier (i.e. f_g<1). The higher the affinity of the particle for butanol, the smaller the contact angle and the smaller the energy barrier required for the butanol to heterogeneously nucleate onto the particle (or equivalently the smaller the value of f_g). In the limit case of a zero contact angle (perfect wetting), the cluster develops in the form of a film onto the surface of the particle seed. If the size of the particle is bigger than the necessary critical cluster size, there is no activation barrier for particle growth (f_g=0). For particle seeds smaller than the critical cluster size though, particle activation requires the formation of a butanol film, the associated energy barrier of which can be derived from geometric considerations:

$$f_g = \begin{cases} 0, & \text{for } X \geq 1 \left(d_p \geq 2r^*\right) \\ (1-X)^2(1+2X), & \text{for } X \leq 1 \left(d_p \leq 2r^*\right) \end{cases} \qquad \text{eq. 7}$$

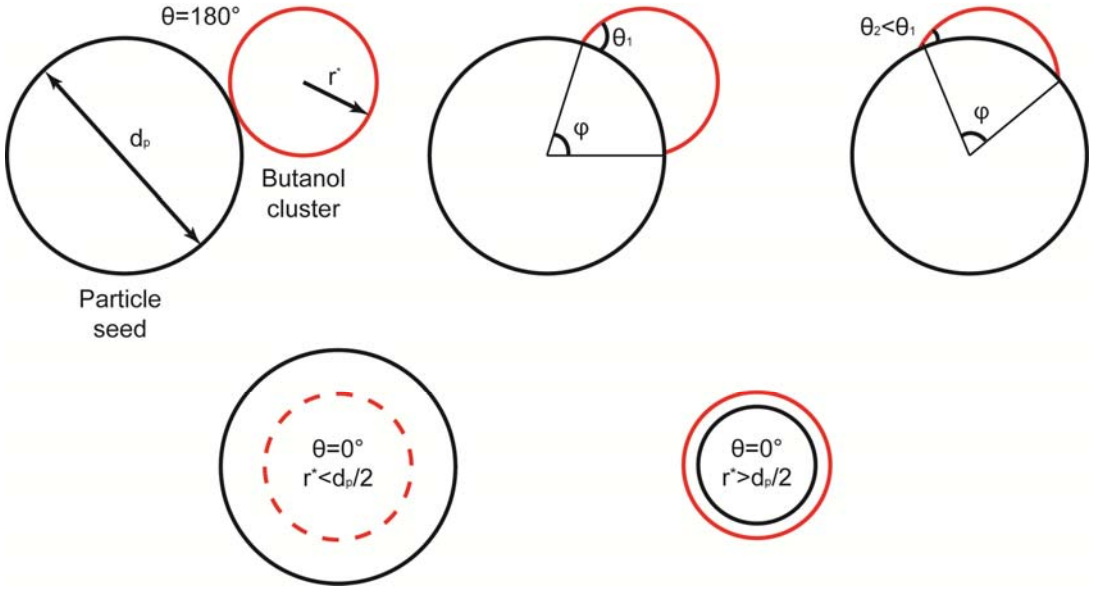

Figure 5: Illustration of the effect of the contact angle on the heterogeneous nucleation mechanism. For perfect wetting ($\theta=0^0$) the activation barrier vanishes when $r^*<d_p/2$ (bottom left), but it remains finite when $r^*>d_p/2$ (bottom right).

The kinetic prefactor has a limited effect on the calculations and generally it is sufficient to be determined within an accuracy of few orders of magnitude [14]. In this study, the approach suggested by Giechaskiel et al. [6] was employed, where the kinetic prefactor is calculated as the product of three factors, namely: the cluster growth rate, R_{growth}, the Zeldovich non-equilibrium homogeneous nucleation factor, Z_{nuc}, and the number of adsorbed vapour molecules per seed particle, F_{ads}. For the shake of simplicity the equations are not reproduced in this report. For the purpose of this study it is sufficient to mention that the calculated prefactors were found to be in the order of $\pi d^2_p 10^{30}$ (d_p expressed in m). For comparison the prefactor suggested by Fletcher [14] in his development of the heterogeneous nucleation model was in the order of $\pi d^2_p 10^{29}$ (d_p expressed in m).

3.1.1.3 CPC detection efficiencies

Once the heterogeneous nucleation rates were calculated for each point of the solution grid (500×500), the probabilities for particle activation were determined from eq. 3, assuming a characteristic time scale of 0.1 s (estimated residence time over the peak saturation ratio). Particles entering the CPC condenser at a given radial bin are assumed to be activated if the activation probability (eq. 3) exceeds 50% anywhere along their axial translocation. The detection efficiency at a given particle size is then calculated as the fraction of the flux-averaged concentration of activated particles, N_d^*, to the total flux-averaged inlet particle concentration, $N_{d,in}$:

$$\eta_d = \frac{\sum_{i=1}^{radialbins} r_i u_i(r_i) N_d^*(r_i)}{\sum_{i=1}^{radialbins} r_i u_i(r_i) N_{d,in}(r_i)} \qquad \text{eq. 8}$$

where $u_i(r_i)$ is the fluid velocity in the i^{th} radial bin. For a parabolic flow $u_i(r_i) = 1 - r_i^2$, whereas for plug flow $u_i(r_i) = const$ (see Section 3.1.2.3). Note that the model developed by Giechaskiel et al. [6] takes also into account diffusional particle losses inside the condenser, by means of solving the mass transfer problem (eq. 1) for the diffusivity of particles. Numerical calculations however suggested that particle losses have insignificant effect (<2 % over the size of interest, ~23 nm) in the calculated detection efficiencies and where therefore neglected.

Table 1 provides information on the geometry of the 3790 and the thermophysical properties employed in the calculations.

Figure 6 shows the effect of contact angles (over the range reported from 3790 calibration measurements [6]) on the calculated detection efficiencies of the 3790_Gold running at the manufacturer's set operating temperatures of 31.7°C (condenser) and 38.3°C (saturator). Also shown in the figure for reference are the detection efficiency requirements laid down in the European regulation (50%±12% at 23±1nm and >90% at 41±1nm). The results illustrate the strong effect of contact angle on the detection efficiency of the 3790. The larger the contact angle, the lower the affinity of the particle for butanol and therefore the lower the detection efficiency. The results also illustrate that the model predicts a 50% counting efficiency at a larger size (25.5 nm in the perfect wetting region) from the targeted regulatory requirement of 23 nm.

Table 1: Geometry of the 3790 condenser and thermophysical properties of butanol employed in the calculations (data for P_{sat}, D_b, ρ_b from [15] and data for σ_{gl} from [16])

Description	Symbol	Unit	Value
3790			
Condenser flowrate	Q	lpm	0.125
Condenser length	L	mm	53
Condenser radius	D_t	mm	4.6
butanol			
Molecular weight	M_b	g/mol	74.123
Density	ρ_b	kg/m^3	$\frac{71.5287}{0.266^{\left(1+\left(1-\frac{T}{563.05}\right)^{0.24419}\right)}}$
Surface tension	$\sigma_{gl}(T)$	N/m, T in K	$\frac{27.18-0.0898(T-273.15)}{1000}$
Saturation pressure	$P_{sat}(T)$	Pa, T in K	$\exp\left(93.173-\frac{9185.9}{T}-9.7464\ln(T)+4.7796\cdot10^{-18}T^6\right)$
Binary diffusion coefficient	$D_b(T,P)$	m^2/s, T in K, P in Pa	$4.26199\cdot10^{-18}\frac{T^{1.75}}{P}$

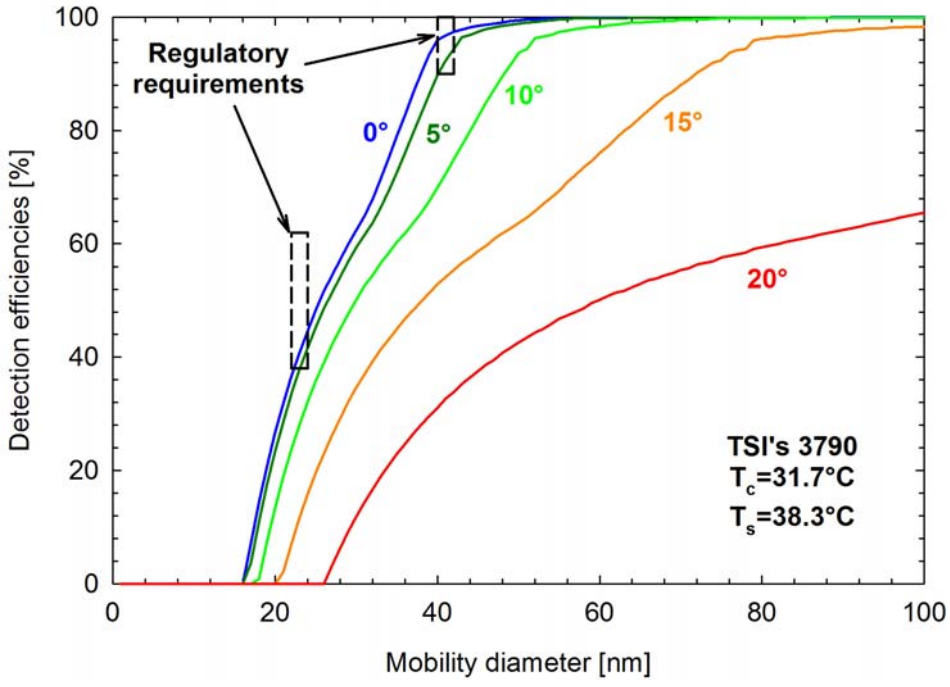

Figure 6: Calculated detection efficiencies of the 3790_Gold CPC at its nominal operating temperatures for contact angles spanning from 0° to 20°. Also shown are the requirements specified by the regulations.

3.1.2 Additional investigations on the numerical model

3.1.2.1 Dependence of surface tension on particle curvature

The basic model employed a fixed value of the surface tension, corresponding to a planar surface. It is expected, however, that the surface tension generally depends on the curvature of the cluster, as was shown in the pioneering works of Gibbs [17] and Tolman R.C. [18]. The influence of curvature (1/*r*) on the surface tension is given by Tolman [18] as:

$$\frac{1}{\sigma_{vl}}\frac{d\sigma_{vl}}{dr}=\frac{\left(\frac{2\delta}{r^2}\right)\left(1+\frac{\delta}{r}+\frac{\delta^2}{3r^2}\right)}{1+\left(\frac{2\delta}{r}\right)\left(1+\frac{\delta}{r}+\frac{\delta^2}{3r^2}\right)} \qquad \text{eq. 9}$$

where δ is a characteristic length (commonly referred to as Tolman length) arising from mathematical consideration and particularly differences in the definition of the cluster dividing surface (equimolar vs minimum surface tension) [19]. The magnitude of the Tolman length is of the order of a molecular diameter (e.g. 0.29 nm for water – [20]), but there is no consensus on the sign which appears to depend on the system under consideration [19].

Under the assumption of a constant Tolman length, eq. 9 yields to a first order approximation [20]:

$$\sigma_{vl}(r)=\frac{\sigma_{vl,planar}}{\left(1+\frac{2\delta}{r}\right)} \qquad \text{eq. 10}$$

In the case of a critical cluster, the radius, r^*, must satisfy the Laplace equation [14]:

$$r^*=\frac{-2\frac{\sigma_{gl,planar}}{\left(1+\frac{2\delta}{r^*}\right)}}{\left[-\frac{\rho_b R_r T}{M_b}\ln(S)\right]}$$

$$\Rightarrow r^*=\frac{2\sigma_{gl,planar}}{\left[\frac{\rho_b R_r T}{M_b}\ln(S)\right]}-2\delta \qquad \text{eq. 11}$$

The size dependence of the liquid-vapour surface tension on the critical radius size, suggests that the microscopic contact angle differs from the macroscopic one (θ_∞). At (mechanical) equilibrium the contact angle is given by Laplace's equation:

$$\cos\theta=\frac{\sigma_{gs}-\sigma_{ls}}{\sigma_{gl}} \qquad \text{eq. 12}$$

where σ_{ij} are the surface tensions between the various phases: vapour (g), liquid (l), and solid (s). For a curved interface, if the curvature dependent vapour-liquid surface tension eq. (10) is used the microscopic microscopic contact angle becomes:

$$\cos\theta = \left(1 + \frac{2\delta}{r^*}\right)\cos\theta_\infty \qquad \text{eq 13}$$

Therefore, the effect of cluster curvature on the surface tension, can be taken into consideration in the heterogeneous nucleation mode (at least to a first order approximation), by replacing eq. 5b with eq. 11 and substituting eq. 10 into eq. 5a, using the microscopic contact angle (eq. 13) for the calculation of the multiplicative factor (eq. 6).

Figure 7 illustrates the effect of Tolman's length, *δ*, on the calculated detection efficiencies. A negative value of δ, increases the critical radius (eq. 11) and most importantly the free energy of formation of a homogeneous nucleating cluster (eq. 5a), thus increasing the energy barrier required to activate the particles. A value of 0.1 nm is sufficient to shift the 50% counting efficiency by 5 (θ=0°) to 7 nm (θ=10°). A positive value of *δ* has the opposite effect. Yet there exists a maximum value of δ at each contact angle above which eq. 12 yields a cosine value of >1. In the calculations, the maximum value of 1 (contact angle 0°) was employed whenever this occurred. This explains the smaller effect of positive *δ* values on the plotted counting efficiencies.

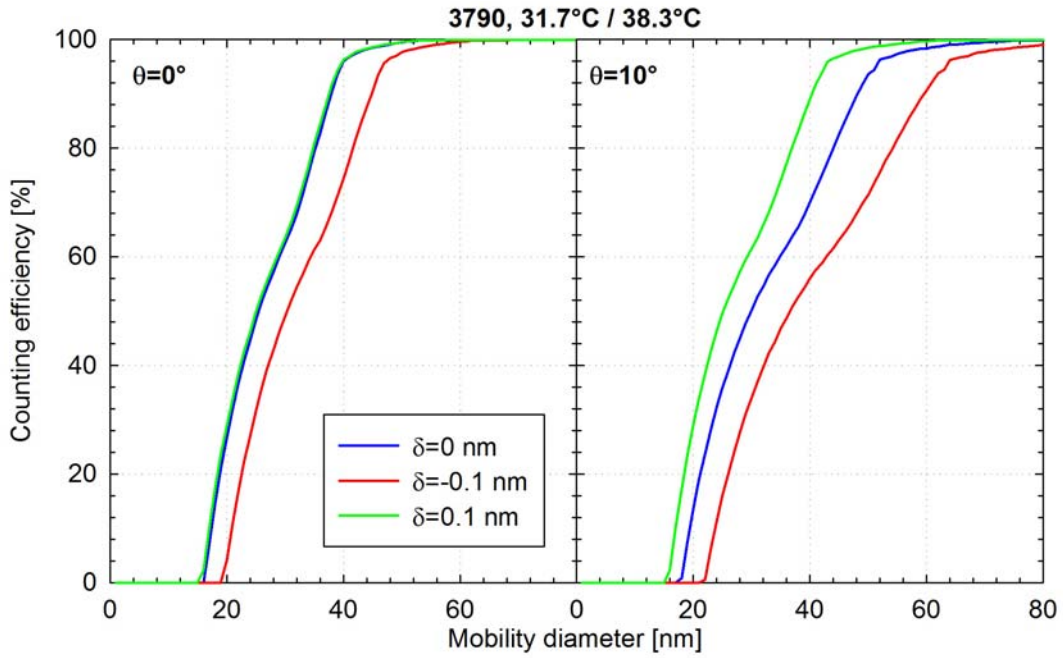

Figure 7: Effect of Tolman's length on the calculated counting efficiencies for perfectly wettable particles (left-hand panel) and for a contact angle of 10° (right-hand panel). A positive value of Tolman's length resulted in a cosine value being greater than 1 in some cases, and accordingly a contact angle of 0° was employed instead.

3.1.2.2 Effect of line tension on the activation probabilities

The heterogeneous nucleation theory, assumes that the critical cluster develops in the form of a spherical cap onto a spherical seed particle. In the interface between the cap and the particle seed (the circumference of the critical cluster), a line tension, σ_t, develops that also contributes to the Gibbs free energy of formation. Lazaridis M. [21], has amended the general heterogeneous nucleation theory to account for the developing line tension. His analysis resulted in the following expressions for the critical Gibbs free energy and contact angle:

$$\Delta G_{het}^{*} = f_g \Delta_{\text{hom}}^{*} - \frac{\sigma_t \pi d_p (1-\cos\phi)}{\tan\phi} + \pi d_p \sigma_t \sin\phi \qquad \text{eq. 14a}$$

$$\Rightarrow \cos\theta = \cos\theta_\infty - \frac{2\sigma_t}{d_p \tan\phi} \qquad \text{eq. 14b}$$

where φ is the angle formed between the circumference of the cap and the center of the particle seed (see Figure 5) and $\cos\theta_\infty$ is the contact angle for the case of negligible line tension.

It can be shown through geometrical considerations that [14]:

$$\tan\phi = \frac{r^* \sqrt{1-\cos^2\theta}}{\frac{d_p}{2} - r^* \cos\theta} \qquad \text{eq. 15}$$

Substitution of eq. 15 into eq. 14b results in a 4th order polynomial with respect to the microscopic contact angle (θ):

$$\begin{aligned}
&\left[(r^*)^2 \sigma_{gl}^2 \left(\frac{d_p}{2}\right)^2 \right] \cos^4\theta \\
&- \left[2(r^*)^2 \sigma_{gl}^2 \left(\frac{d_p}{2}\right)^2 \cos\theta_\infty \right] \cos^3\theta \\
&+ \left[\sigma_t^2 (r^*)^2 - (r^*)^2 \sigma_{gl}^2 \left(\frac{d_p}{2}\right)^2 + (r^*)^2 \sigma_{gl}^2 \left(\frac{d_p}{2}\right)^2 \cos^2\theta_\infty \right] \cos^2\theta \\
&+ \left[-r^* d_p \sigma_t^2 + 2(r^*)^2 \sigma_{gl}^2 \left(\frac{d_p}{2}\right)^2 \cos\theta_\infty \right] \cos\theta \\
&+ \left[\sigma_t^2 \left(\frac{d_p}{2}\right)^2 - (r^*)^2 \sigma_{gl}^2 \left(\frac{d_p}{2}\right)^2 \cos^2\theta_\infty \right] = 0
\end{aligned} \qquad \text{eq. 16}$$

The above equation allows for the calculation of the microscopic contact angle (θ) for a given macroscopic contact angle (θ_∞), line tension (σ_t) and particle diameter. The critical radius is still calculated through eq. 5b. Equation 16 has generally two real solutions in the vicinity of $\cos\theta_\infty$ corresponding to positive ($\cos\theta<\cos\theta_\infty$) and negative ($\cos\theta<\cos\theta_\infty$) line tension ($\sigma_t$).

The effect of line tension on the calculated counting efficiencies of the 3790_Gold, operating at its nominal condenser and saturator temperatures, is illustrated in Figure 8. The contribution of line tension becomes more important at higher contact angles. A line tension of $\pm 2\times10^{-12}$ N (a value that is two orders of magnitude lower from the figure suggested by Scheludko et al. [22] for water condensation on hexadecane) is sufficient to shift the 50% counting efficiency by 4-7 nm at 10° contact angle. Yet, in the case of perfectly wettable particles, the calculated detection efficiencies are indistinguishable over this range of line tension values.

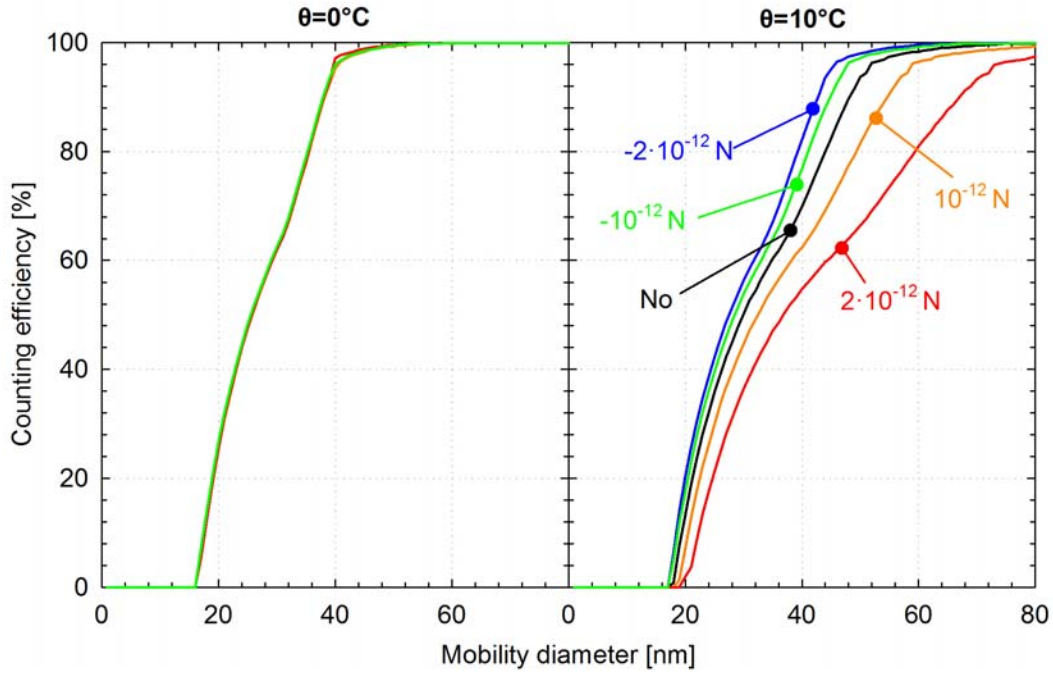

Figure 8: Effect of line tension on the calculated counting efficiencies at the nominal operating temperatures of the 3790_Gold CPC, at contact angles of 0° (left-hand panel) and 10° (right-hand panel).

3.1.2.3 Effect of inlet temperature and velocity profiles

The basic model assumes a hydrodynamically fully developed velocity profile (parabolic Hagen-Poiseuille), uniform fluid temperature, and uniform, saturated, n-butanol concentration at the condenser inlet. Such conditions would probably prevail in a cylindrical geometry with a long saturator tube. However, CPC designs may introduce bends, contractions, or other deviations from a cylindrical geometry. The effect of different CPC geometries was assessed by considering a non-uniform condenser inlet temperature and a constant inlet velocity (plug flow).

The effect of temperature inhomogeneities at the inlet (for a Hagen-Poiseuille flow) was quantified by considering a 2° temperature difference between the inlet centerline temperature, $T_{in}(r=0)$, and the inlet wall temperature $T_{in}(r=1)$. As in the basic model, the n-butanol inlet concentration was taken to be the concentration of satured n-butanol vapours at the non-uniform inlet temperature. The physical properties of the vapour and the carrier gas were evaluated at the mean inlet temperature T_{0m}. The inlet concentration, cf. eq. (2a), was fitted to a second degree polynomial to simplify the calculation. The inlet temperature and concentration profiles used in the calculations were:

$$T_{in}(r)[°C] = 39.37 - 2r \qquad \text{eq. 17a}$$

$$C_{b,sat}(T_{in}(r))\left[g/m^3\right] = 69.24\left(1 - 0.119r + 0.006r^2\right) \qquad \text{eq. 17b}$$

Accordingly, the inlet centerline temperature was $T_{in}(r=0)$=39.37°C and the inlet wall temperature $T_{in}(r=1)$=37.37°C. To ensure a consistent comparison with the results of the basic model the inhomogeneous inlet temperature and concentration profiles were chosen such that their mean values equal the values of the basic model, i.e., the flux-average temperature and concentration were T_{0m} = 38.3°C and C_{0m} =64.94 g/m^3. Details of the

necessary modifications of the analytical solution for inlet profiles specified by a polynomial of degree k may be found in Housiadas et al. [23].

Figure 9 presents the resulting n-butanol saturation ratio in the condeser, whereas Figure 10 compares calculated counting efficiencies, at two contact angles, of the 3790_Gold CPC for unifom inlet profiles (temperature and n-butanol concentration, basic model) to the counting efficiencies for non-uniform profiles.

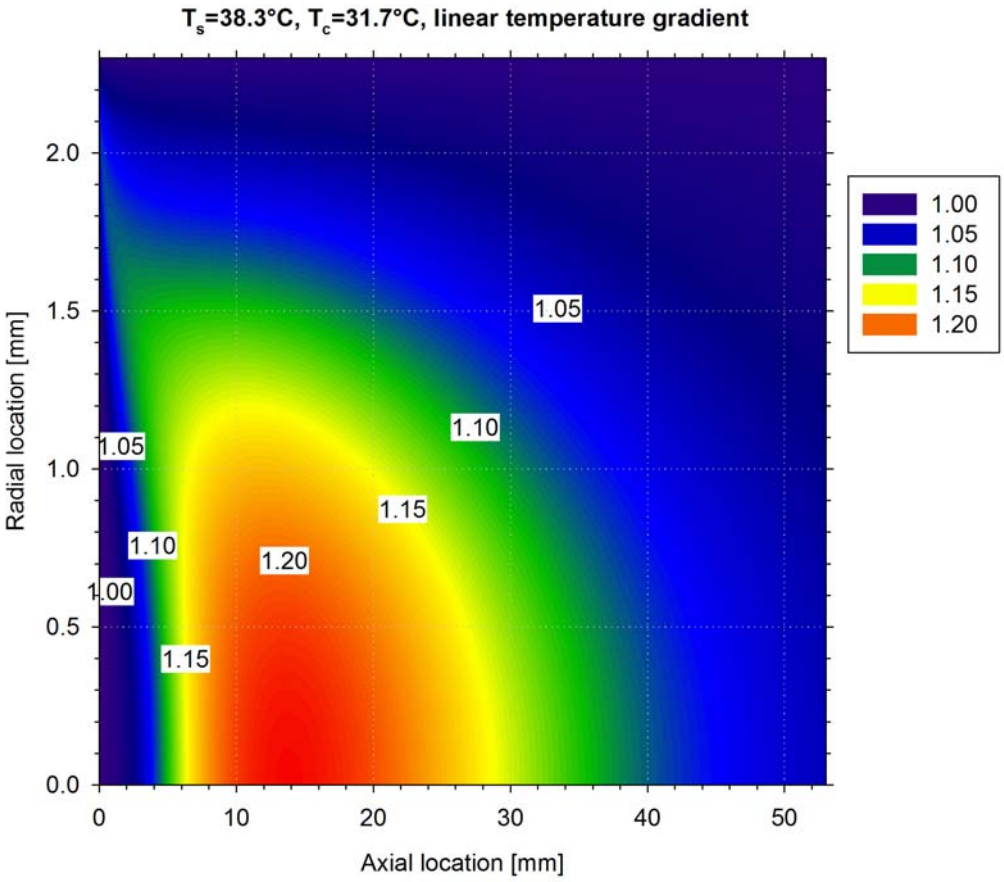

Figure 9: Calculated saturation ratio profile inside the condenser at the nominal operating temperatures of the 3790_Gold CPC, assuming a linear temperature gradient at the inlet of the condenser resulting in a two degrees temperature difference between the wall (lowest temperature) and the center rod (highest temperature).

A detailed comparison of Figure 4 and Figure 9 suggests some subtle but systematic changes in the saturation ratio profile. More specifically, the peak saturation ratios for non-uniform temperature profile are slightly higher near the wall and vice versa near the condenser center line. Since the activation of large particles requires lower saturation ratios and the counting efficiencies effectively increase with the area within which the critical saturation ratio for the specific size is achieved, a non-linear temperature profile is expected to result in relatively higher counting efficiencies at large sizes and lower efficiencies at smaller sizes, as evident in Figure 10.

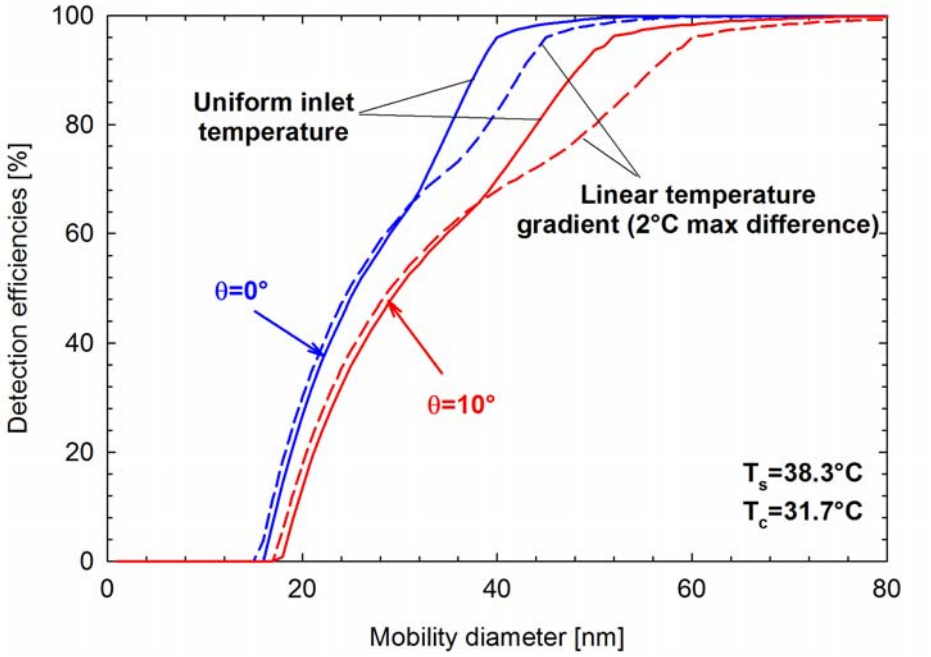

Figure 10: Calculated counting efficiencies of the 3790_Gold for contact angles of 0° (blue lines) and 10° (red lines) assuming uniform temperature profile (solid lines) and a linear temperature gradient (dashed lines) at the inlet of the condenser.

Changes of the inlet velocity profile due to geometry of the CPC were considered by taking the saturator inlet velocity to be uniform. As in the basic model, the uniform velocity was imposed to be the average velocity u_{ave}=0.1254 m/s, the uniform temperature T_{0m}=38.3°C, and n-butatol concentration C_{0m} =64.94 g/m^3. The change from the parabolic velocity to the constant average velocity in eq. 1 requires a change of the spatial scaling of the axial variable to twice the scaling shown in eq. 1b. This change is necessary because the maximum (centerline) velocity in parabolic flow is $u_{\max} = 2u_{ave}$. For a constant velocity, the analytical solution for the dimensionless concentration $\vartheta(r,x)$ is

$$\vartheta(r,x) = 2\sum_{n=1}^{\infty} \frac{J_0(\lambda_n r)}{\lambda_n J_1(\lambda_n)} \exp\left(-\lambda_n^2 x\right) \qquad \text{eq. 18}$$

where $\vartheta(r,x)$ refers to heat or mass transfer according to eqs. (1b, 1c), $J_i(z)$ is the i^{th} order Bessel function of the first kind, and λ_n are the zeroes of the 0th order Bessel function of the first kind $J_0(z)$. As in the basic model, 150 terms were kept in the infinite sum. Figure 11 and Figure 12 summarize the calculation results.

Comparison of Figures 4 and 11 shows that for a uniform inlet velocity profile the peak saturation ratio becomes slightly higher along all radial locations. Consequently, particle activation via heterogeneous nucleation would be easier for a uniform inlet velocity. Figure 12, where counting efficiencies for the two inlet profiles are compared, confirms this observation, i.e., that plug-flow counting efficiency curves are above the parabolic-flow efficiency curves (higher counting efficiency for a given particle diameter).

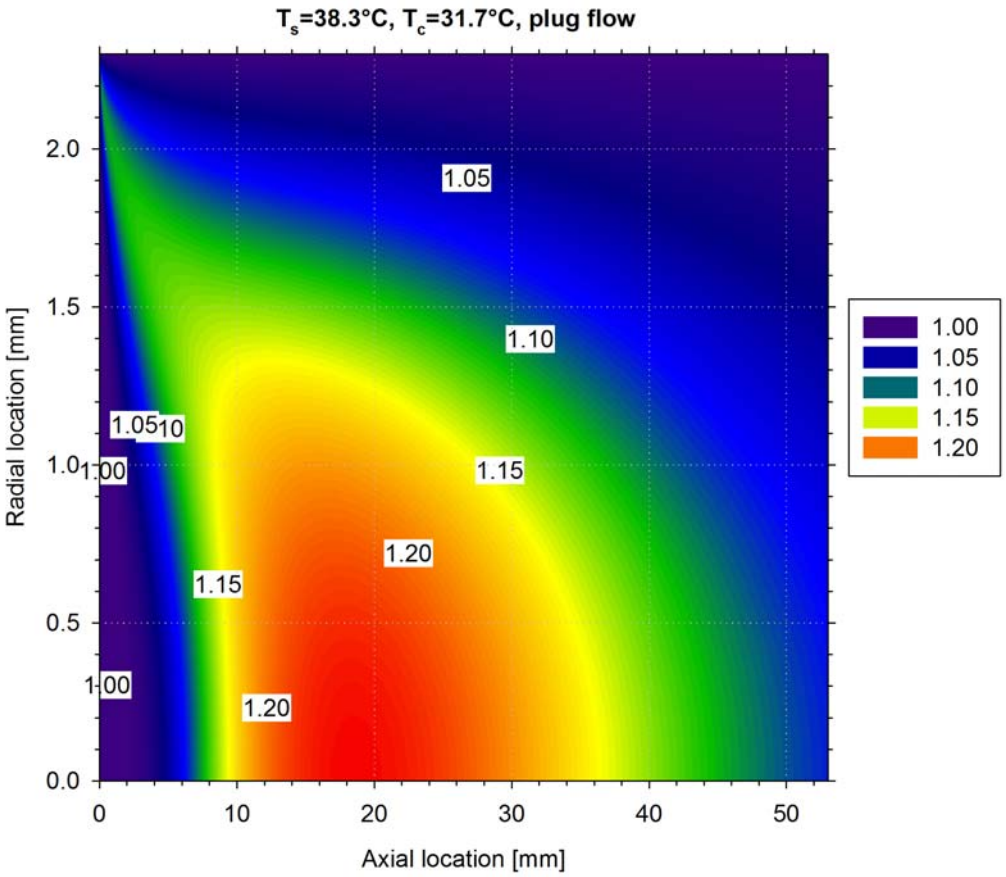

Figure 11: Calculated saturation ratio profile inside the condenser at the nominal operating temperatures of the 3790_Gold CPC, assuming a plug flow.

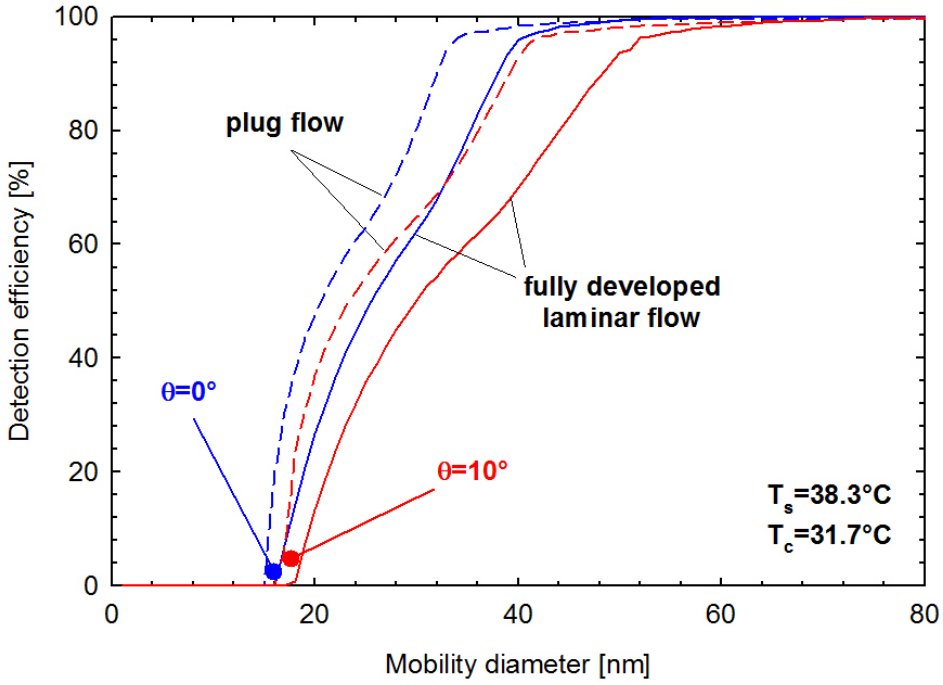

Figure 12: Calculated counting efficiencies of the 3790_Gold for contact angles of 0° (blue lines) and 10° (red lines) assuming fully developed laminar flow (solid lines) and plug flow (dashed lines) in the condenser.

3.1.2.4 Effect of particle charge state

It was long known that ions can enhance the homogeneous nucleation of vapours [24]. An approximate thermodynamic expression for ion induced homogeneous nucleation was already developed more than a century ago [25, 26]. Under the assumption of a charged ion surrounded by a layer of condensed vapour, the Gibbs free energy of formation of a droplet of radius r is reduced by:

$$G_{el,\hom} = \frac{q^2}{8\pi\varepsilon_o}\left(\frac{1}{\varepsilon_g}-\frac{1}{\varepsilon_l}\right)\left(\frac{1}{r}-\frac{1}{r_0}\right) \qquad \text{eq. 19}$$

where r and r_0 are the radii of the droplet and the ion, respectively, q is the charge on the ion, while ε_0 is the vacuum permittivity and ε_l (ε_g) the dielectric constant of the liquid (vapor) phase.

Accordingly the saturation ratio at which homogenous nucleation of butanol vapours occurs, reduces to [26, 27]:

$$\ln S = \frac{2\sigma_{gl}M_b}{\rho_b R_g T r^*} - \frac{q^2 M_b}{32\pi^2\rho_b R_g T\varepsilon_0 \left(r^*\right)^4}\left(1-\frac{1}{\varepsilon_l}\right) \qquad \text{eq. 20}$$

In writing eq. 20 we have taken the vapor-phase dielectric constant to be unity (valid to a good approximation). Figure 13 compares the critical saturation ratios for homogeneous nucleation and ion-induced nucleation of butanol vapours (ε=18) at the nominal saturator temperature of the 3790 CPC (38.3°C). The calculations clearly show that the effect of charges becomes important only at small particle sizes (less than 0.1% reduction in the saturation ratio at 8 nm).

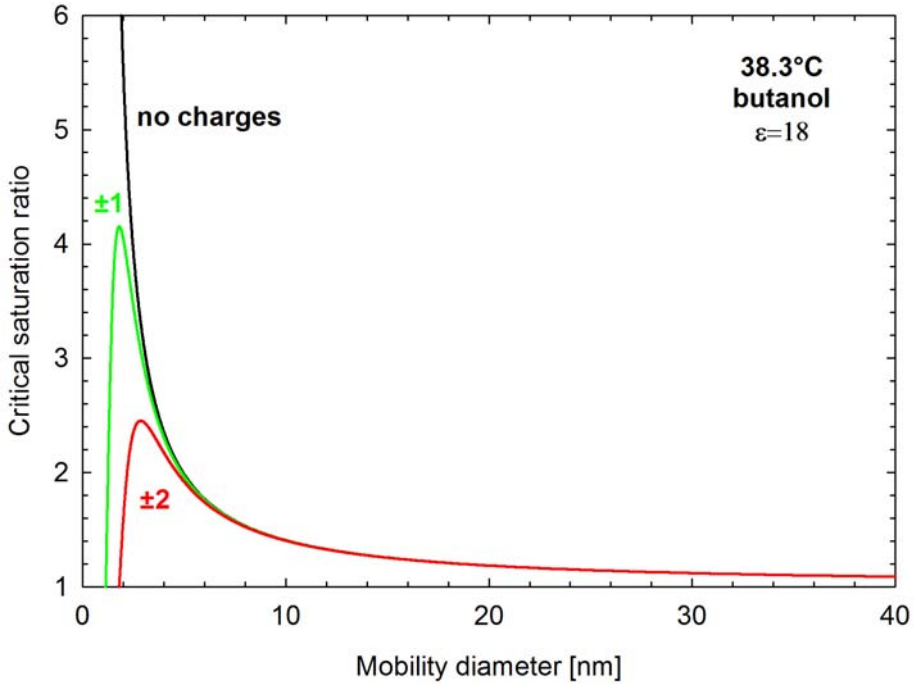

Figure 13: Critical saturation ratios for homogeneous nucleation (Kelvin effect) and ion-induced homogeneous nucleation of butanol vapours at the nominal saturator temperature of the 3790 CPC.

The problem of heterogeneous nucleation of vapours onto charged particles is far more complicated as it requires consideration of the complex electric field forming around the particle [28]. In the case of small contact angles though, it is anticipated that eq. 20 is approximately valid if one replaces r_0 with the particle radius [29], and combination of the Thompson and Fletcher theories were shown to adequately explain experimental data. Overall, it is expected that the effect of particle charge on the detection efficiencies of the 3790 CPC should be insignificant, at least over the size range of interest (>10 nm).

3.1.2.5 Particle growth

The heterogeneous nucleation theory developed by Fletcher [14] and employed in the calculations presented in this report, considers the idealized case of the activation of an isolated particle in a surrounding gas held at constant supersaturation of given vapours. In reality, the saturation ratio profile inside the condenser of the CPC shows a strong spatial variation (Figure 4). Furthermore, the condensation of vapours onto the particle may affect the saturation ratios in the vicinity of the particle due to both a) latent heat release and b) vapour depletion and this can affect the activation of neighbour particles.

In order to investigate the significance of such effects on the counting efficiencies of the CPC, some condensational growth calculations were performed. To simplify the calculations, the condensational growth problem was decoupled from the heat and mass transfer problem (eq. 1). That is, the growth of particles was investigated over the temperature and saturation profile calculated with eq. 1.

According to Fuchs [30] the rate of particle growth is given by [31, 32]:

$$\frac{d\left(d_p\right)}{dt} = \frac{4D_b M_b}{R_g \rho_p d_p}\left(\frac{p_\infty}{T_\infty} - \frac{p_d}{T_d}\right)\phi \qquad \text{eq. 21}$$

where p_d and p_∞ are the vapour pressures at the droplet surface and the surroundings while T_d and T_∞ the corresponding temperatures. The Fuchs correction factor, φ, accounts for the lower rates of growth of particles in the transition and free molecule regimes:

$$\phi = \frac{2\lambda + d_p}{d_p + 5.33\left(\frac{\lambda^2}{d_p}\right) + 3.42\lambda} \qquad \text{eq. 22a}$$

where λ is the mean free path between molecular collusions, which for air can be calculated as [33]:

$$\lambda[nm] = 66.4\left(\frac{101}{P}\right)\left(\frac{T}{293}\right)\left(\frac{1+\frac{110}{293}}{1+\frac{110}{T}}\right) \qquad \text{eq. 22b}$$

The temperature at the droplet is affected by both the heat acquired by the droplet due to condensation and that lost by conduction to the cooler surroundings. Balancing of these two heat transfer mechanisms yields a steady-state temperature elevation that can be calculated from the following expression [31, 32]:

$$T_d - T_\infty = \frac{D_b M_b H_b}{R_g k_{air}} \left(\frac{p_d}{T_d} - \frac{p_\infty}{T_\infty} \right) \quad \text{eq. 23}$$

where H_b is the butanol latent heat of evaporation and k_{air} is the thermal conductivity of the carrier gas (air).

The onset of particle growth was considered to be the point at which the particle activated inside the CPC condenser. Since the condensation growth model described by eq. 18 to eq. 23 is based on thermodynamic considerations only, particle activation for these calculations was assumed to occur at saturation ratios above the Kelvin ratio, K_R:, (eq. 5b):

$$K_R = \frac{p_d}{p_{b,sat}} = \exp\left(\frac{4\sigma_{gl} M_b}{\rho_b R_g T_d d_p} \right) \quad \text{eq. 24}$$

This assumption was necessary, since the use of a potentially lower droplet vapour pressure determined from heterogeneous nucleation considerations in the system of eq. 21 to eq. 23 could result in droplet shrinkage.

For the solution of the ordinary differential equation described in eq. 21, the 4th order Runge Kutta method was employed [34]. Equation 23 was solved implicitly at each calculation step using the secant method [34].

Figure 14 shows the calculated distribution of droplet sizes at the exit of the condenser at the nominal operating temperatures of the 3790_Gold CPC for four selected sizes. The results suggest that particles grow to sufficiently large sizes to be effectively detected in the optical sensor (capable of sensing droplets larger than circa 0.5 μm – [32]). Figure 15 shows the calculated time evolution of droplets following activation of 23 nm particles at the nominal operating temperatures of the 3790_Gold for two extreme cases, namely a) particles entering at the centre of the condenser and b) particles entering at the outermost radial location at which 23 nm particles activate. In both cases, the particles grow to super micron sizes in less than 5 ms.

Some calculations were also performed to investigate whether the quantity of butanol vapours available in the condenser suffices for the calculated droplet growths. The mass of vapours that condenses on particles entering the condenser at a given radial location was calculated as:

$$C_{b,depleted} = N_{d,in} \frac{\pi d_{droplet}^3}{6} \rho_b \quad \text{eq. 25}$$

where $d_{droplet}$ is the diameter of the droplet which was assumed to instantaneously reach the peak size calculated at the exit of the condenser (worst-case scenario). The results of these calculations are plotted in Figure 16. The left-hand panel depicts the fraction of the total available vapour mass that is consumed at the point where particle activation occurs (resulting from the solution of the mass transfer problem – eq. 1 and eq. 2). The right-hand panel illustrates the associated reduction in the local saturation ratio. The results suggest that the larger the particle seed size the larger the fraction of available butanol that will be consumed. This is mostly due to the larger size of the droplet (Figure 14) and to a much lesser extend due to the lower amount of butanol available at the lower supersaturations at which larger particles activate. A 3% reduction in the butanol vapour concentration will result

in a similar reduction of the local saturation ratios (lying in the range of 1 to 1.25 at the nominal operating temperatures of the 3790).

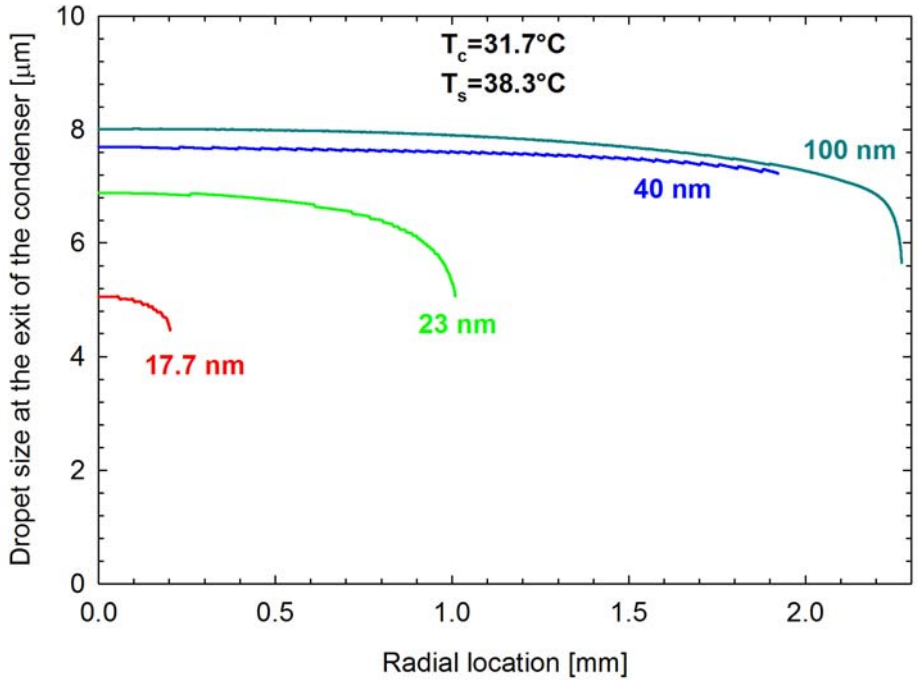

Figure 14: Calculated distribution of droplet sizes at the exit of the 3790 condenser at the nominal operating temperatures, for four selected particle sizes.

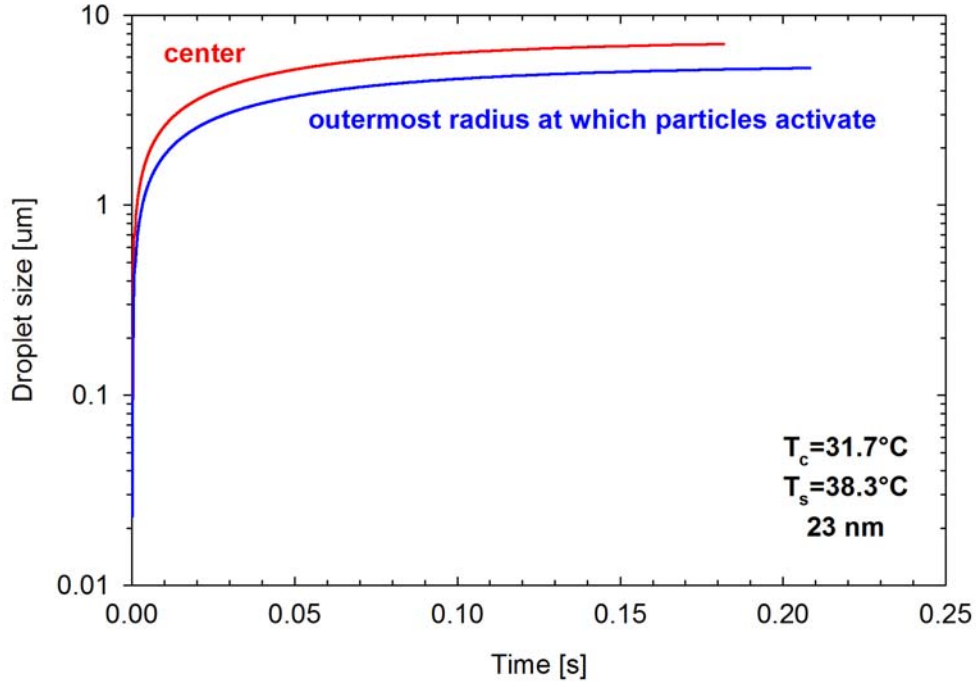

Figure 15: Time evolution of droplet size upon activation of 23 nm particles at the nominal operating temperatures of the 3790 CPC. Two extreme cases are shown, corresponding to particles entering at the center of the condenser and the outermost radial location at which 23 nm particles activate.

Condensation growth can also reduce the saturation ratios in the vicinity of the point at which a particle activates through convection/conduction of the heat released by the warmer (eq. 23) droplet. Figure 17 shows the calculated temperature increase at the droplet surface at the point where the particle activates inside the condenser. Again the calculations where performed assuming the droplet grows instantly, but as noted by Hinds W.C. [31] the droplet size has minimal effect in the calculations. The results suggest that the maximum temperature increase occurs during activation of the smallest particles and is approximately 1.5°C. The right-hand panel of Figure 17 also shows the decrease in the local saturation associated with the temperature rise through condensation. The maximum reduction (occurring during activation of the smallest detectable size ~17.5 nm) is calculated to be 9.3%.

Whether or not the calculated reductions in the local saturation ratios will affect the activation of neighbour particles will depend on the relative distance between the particles. Assuming a maximum concentration of 10000 #/cm^3 and that the particles are uniformly distributed in the condenser, the mean distance between particles is:

$$\sqrt[3]{0.0001cm^3} = 0.0464cm = 464\mu m \qquad \text{eq. 26}$$

This figure is approximately 60 times larger the maximum droplet size (Figure 14) and as such it can be speculated that the activation of a given particle can not affect the activation of other particles in the neighbour. Overall, the calculations suggest that practically, all activated particles are effectively counted.

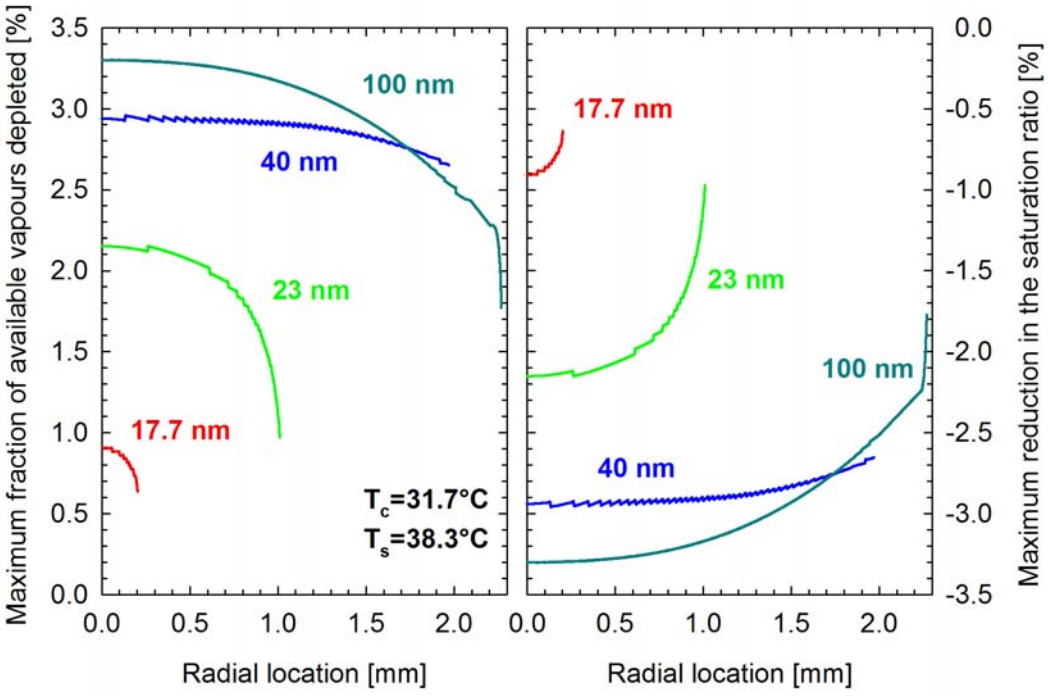

Figure 16: Maximum estimated fraction of butanol depleted (left-hand panel) and associated reduction in the local saturation ration (right-hand panel) during activation of particles inside the condenser of the 3790_Gold at its nominal operating temperatures.

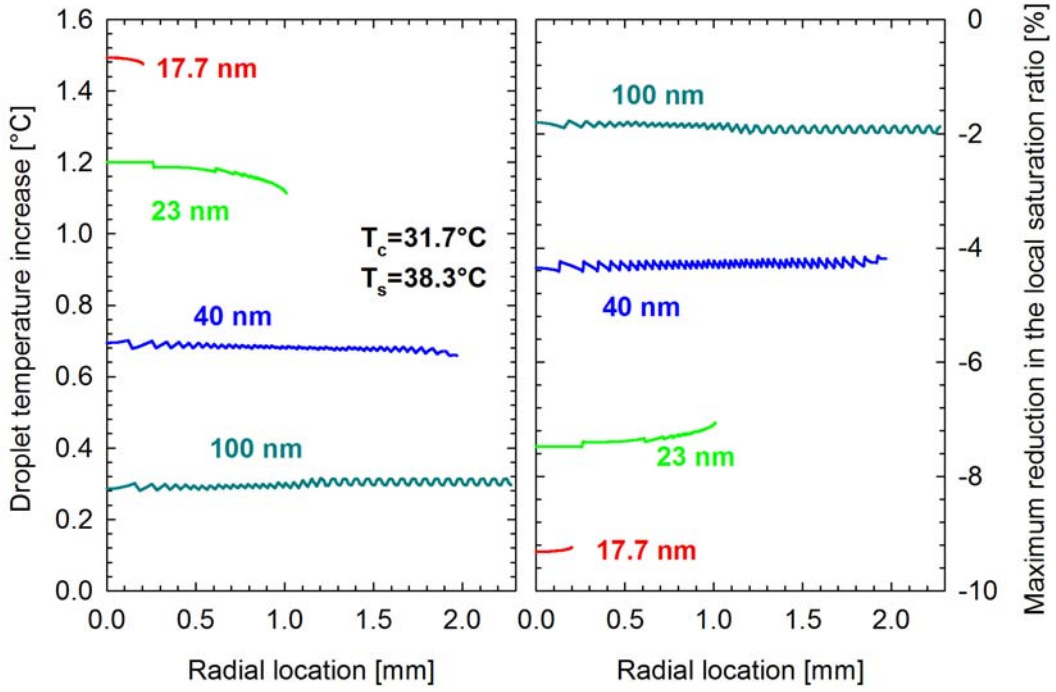

Figure 17: Calculated temperature increase at the droplet surface (left-hand panel) and associated reduction in the local saturation ration (right-hand panel) during activation of particles inside the condenser of the 3790_Gold at its nominal operating temperatures.

3.2 Simulated Tandem DMA responses

Some numerical calculations were also performed in order to estimate the charging state of the particles classified in the TDMA setup (e.g. Figure 2 and Figure 3). The calculation procedure is illustrated in Figure 18.

Starting from the polydisperse size distribution produced by the generator (as measured with a TSI 3936L10 SMPS), the distribution of charges acquired in the first neutralizer was calculated (Figure 18b). For these calculations the approximate formulas derived by Wiedensohler A. [35], and are also used in the TSI data inversion software, were employed (Figure 19).

In a second step the size distributions of negatively charged particles were convoluted with the transfer function of the first DMA at the selected (positive) centre rod voltage (Figure 18c). Since the DMA classifies particles according to their electrical mobility, Z_p, the size distributions of charged particles were reallocated on the electrical mobility axis according to their number, n, of elementary electrical charges, e:

$$Z_p = \frac{neC_C}{3\pi\mu d_p} \qquad \text{eq. 27}$$

where μ is the viscosity of air and C_C is the Cunningham slip correction factor [36]:

$$\mu[Pa \cdot s] = 1.8203 \cdot 10^{-5}\left(\frac{T}{293.15}\right)^{1.5}\frac{403.55}{T+110.4} \qquad \text{eq. 27a}$$

$$C_C = 1 + 2\frac{\lambda}{d_p}\left(1.142 + 0.558\exp\left(\frac{-0.999 d_p}{2\lambda}\right)\right) \qquad \text{eq. 27b}$$

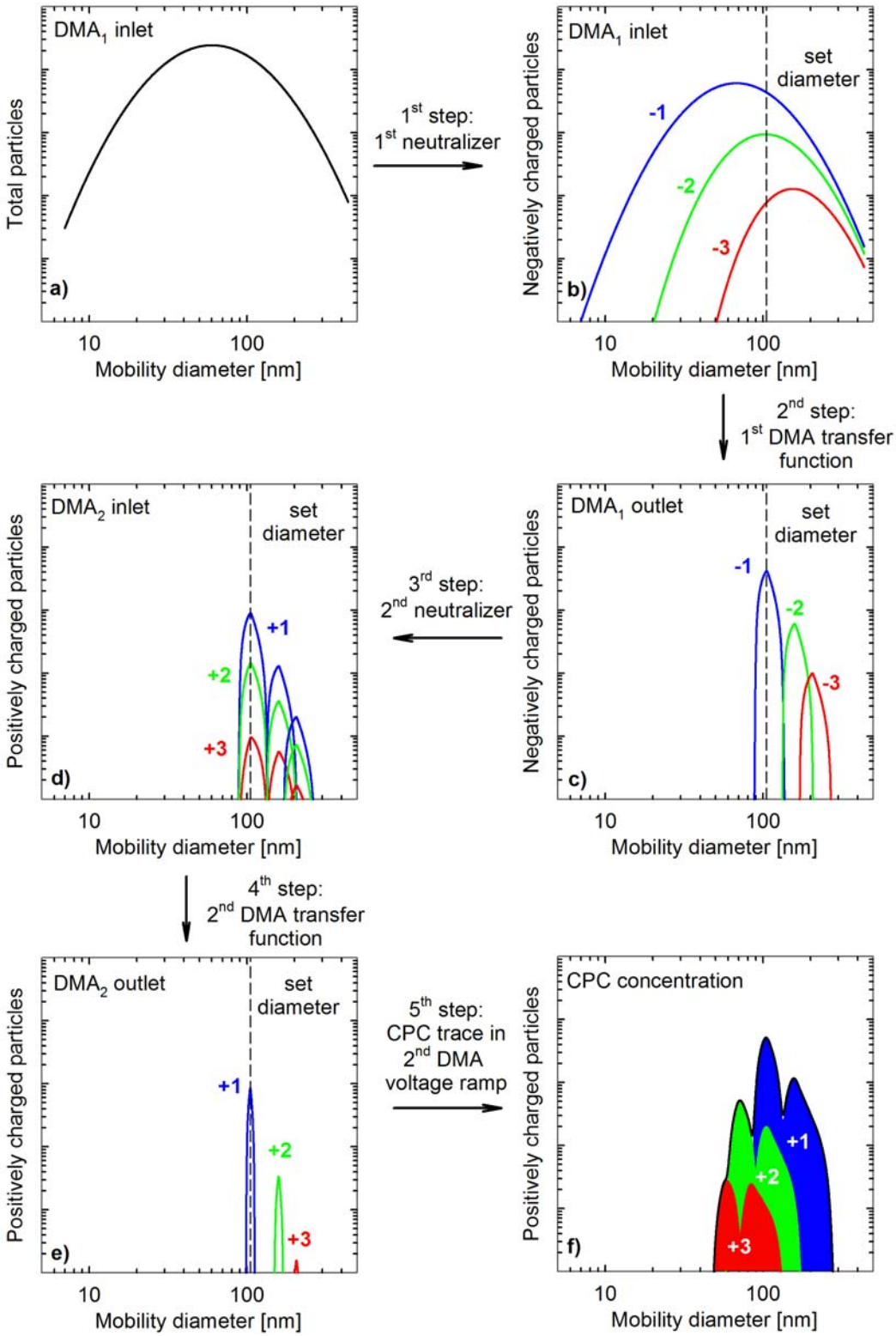

Figure 18: Calculation procedure for the simulation of the TDMA responses.

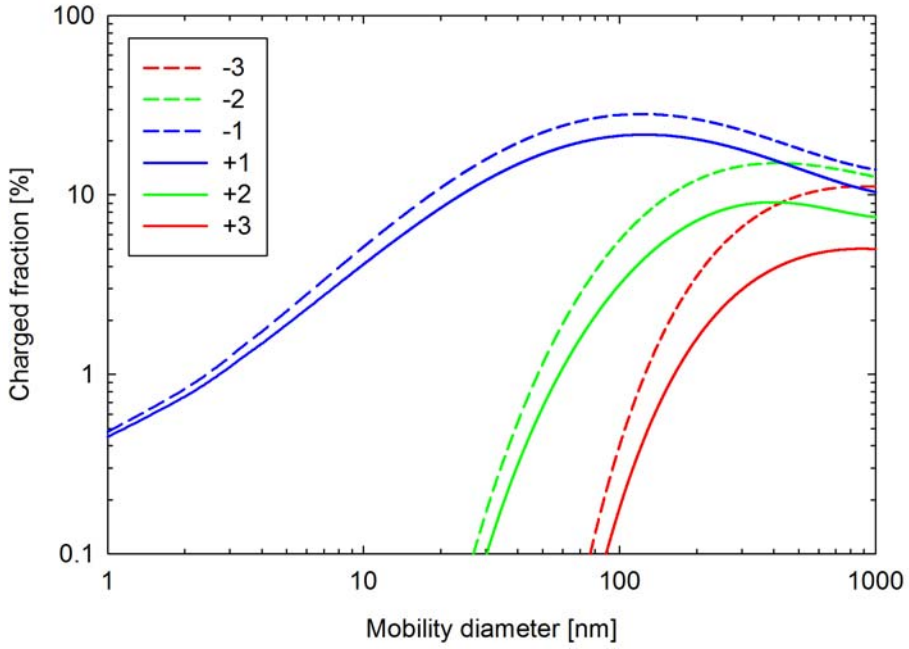

Figure 19: Distribution of charges acquired in the neutralizer according to Wiedensohler A. [35].

The transfer functions were calculated using the semi-analytical solution derived by Stolzenburg [37] that takes into account diffusion broadening (Figure 20):

$$\Omega\left(\tilde{Z}_p\right)=\frac{\sigma}{\sqrt{2}\pi\left(1-\delta\right)}\left\{\begin{array}{l}\varepsilon\left[\frac{\tilde{Z}_p-\left(1+\beta\right)}{\sqrt{2}\sigma}\right]+\varepsilon\left[\frac{\tilde{Z}_p-\left(1-\beta\right)}{\sqrt{2}\sigma}\right]\\-\varepsilon\left[\frac{\tilde{Z}_p-\left(1+\beta\delta\right)}{\sqrt{2}\sigma}\right]-\varepsilon\left[\frac{\tilde{Z}_p-\left(1-\beta\delta\right)}{\sqrt{2}\sigma}\right]\end{array}\right\} \qquad \text{eq. 28}$$

with:

$$\varepsilon\left(x\right)=\frac{2x}{\sqrt{\pi}}\int_0^x e^{-t^2}dt+\frac{1}{\sqrt{\pi}}e^{-x^2} \qquad \text{eq. 28a}$$

$$\beta=\frac{Q_a+Q_s}{Q_{sh}+Q_e} \qquad \text{eq. 28b}$$

$$\delta=\frac{Q_s-Q_a}{Q_s+Q_a} \qquad \text{eq. 28c}$$

$$\tilde{Z}_p=\frac{Z_p 4\pi L_{DMA}V_0}{\left(Q_{sh}+Q_e\right)\ln\left(\frac{r_2}{r_1}\right)} \qquad \text{eq. 28d}$$

$$\sigma = \sqrt{G\tilde{Z}_p \ln\left(\frac{r_2}{r_1}\right)\frac{k_b T}{neV_0}}$$ eq. 28e

$$G = \frac{4(1+\beta)^2}{1-\frac{r_1^2}{r_2^2}}\left\{I_\gamma\left(\frac{r_1^2}{r_2^2}\right)+\left[\frac{\left(r_2^2-r_1^2\right)}{2(1+\beta)Lr_2}\right]^2\right\}$$ eq. 28f

$$I_\gamma(x) = \frac{\left[\frac{1}{4}(1-x^2)(1-x)^2+\frac{5}{18}(1-x^3)(1-x)\ln(x)+\frac{1}{12}(1-x^4)\ln^2(x)\right]}{(1-x)\left[-\frac{1}{2}(1+x)\ln(x)-(1-x)\right]^2}$$ eq. 28g

where Q_a, Q_s, Q_{sh} and Q_e are the operating flows of the DMA (aerosol inlet flow, extracted sample flow, sheath flow and excess flow), L_{DMA} is the length of the centre rod, r_1 and r_2 are the inner and outer radii of the annular space of the DMA classification region and V_0 is the centre rod voltage.

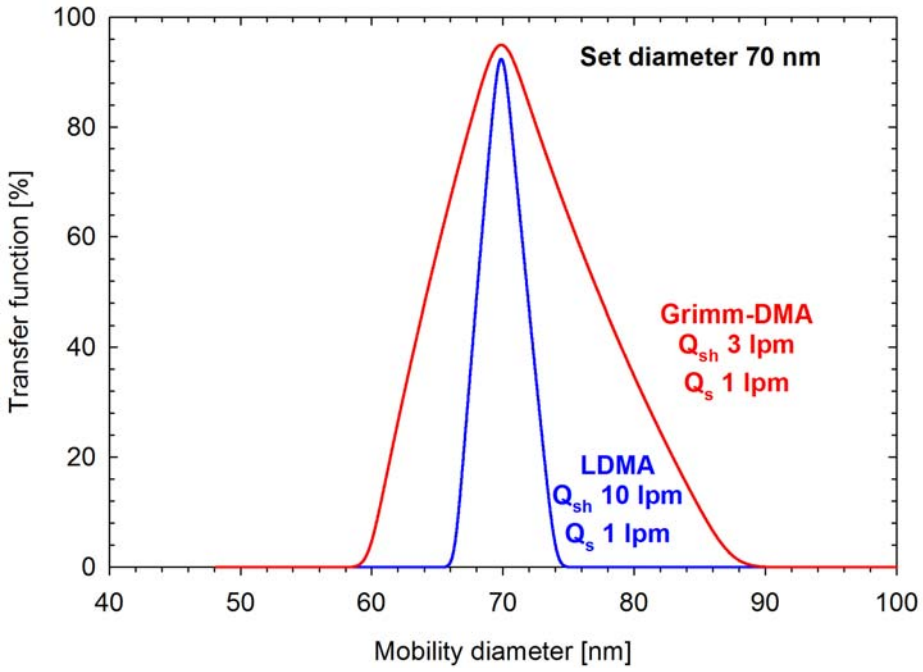

Figure 20: Calculated transfer functions for the Grimm-DMA (red line) and the LDMA (blue line) at the operating flowrates employed in this study and for a selected classified size of 70 nm, using the semi-analytical expression of Stolzenburg [37].

The negatively charged particles exiting the first DMA were then neutralized again in the second bipolar charger, and the fraction of positively charged particles was recalculated (Figure 18d – [35]). The last stage of the calculations consisted of convoluting the distribution

of positively charged particles entering the second DMA with the transfer function of the second DMA (Figure 20) for each negative centre rod voltage applied. This allowed for a reconstruction of the CPC trace over a TDMA scan as well as for the estimation of the fraction of multiply charged particles in the aerosol sampled by the CPC at each instant of the TDMA scan (Figure 18f).

Particle losses in the TDMA system were not taken into account in these calculations but their effect is expected to be small due to the large particle sizes employed in these particular tests (set diameter at ~100 nm).

4 RESULTS

4.1 DMA Calibration

Figure 21 illustrates a typical size distribution of the nebulized 500 nm PSL particles as measured with the TSI 3936L10 SMPS. Both the multiply-charged corrected and the uncorrected distributions are shown for comparisons. The 500 nm PSL spheres can be clearly distinguished from the background, polydisperse distribution of impurities in the diluted water suspensions. A smaller peak occurring at somehow larger sizes (~640 nm) most probably corresponds to doublets of PSL spheres. In fact, theoretical calculations [38] suggest that the mobility diameter of a dimer composed of two 500 nm spheres is 645 nm, for motion parallel to the symmetry axis joining the two monomer centers of mass. These results provide evidence of particle alignment inside the DMA [39] at least at the elevated voltage required to classify doublets of 500 nm spheres (~7400 V).

The spikes occurring at smaller particle sizes in the uncorrected distribution (i.e. the one resulting assuming that all particles are singly charged) correspond to multiple charged PSL spheres. The multiple-charge correction algorithm, effectively reduces these spikes. Interestingly though, some distinct spikes can still be identified, suggesting that the inversion algorithm underestimates the fraction of multiply charged particles.

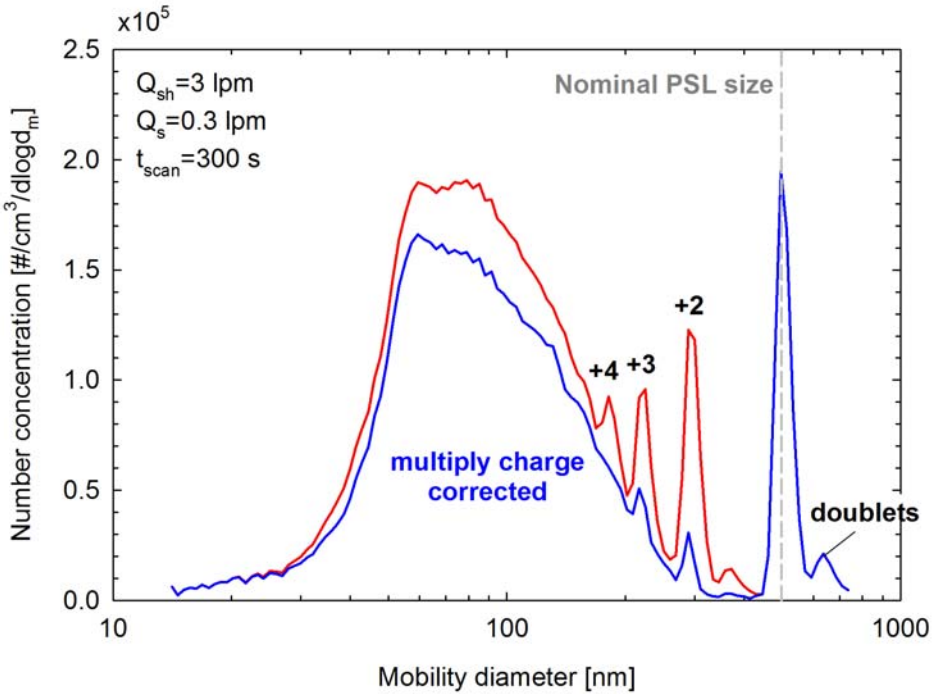

Figure 21: Typical size distributions of nebulized 500 nm PSL particles measured with the TSI's 3936L10 SMPS. Both the multiply-charged corrected (blue line) and the uncorrected (red line) distributions are shown.

The SMPS distributions do not provide however accurate information on the sizing capabilities of the LDMA due to the limitation of 64 size bins per decade inherent in the TSI's data inversion algorithm and to a lesser extent (owing to the long scan times employed) due to inaccuracies related to the scanning mode of operation [12, 11]. Figure 22 shows instead the measured concentrations of PSL spheres over 4 repetitions of step voltage changes

around the nominal peak. The calculated geometric mean diameter was found to be 499.8 (±0.7) nm (where the error-band next to the numbers presented hereinafter corresponds to ± one standard deviation). Stolzenburg's transfer function calculated at the operating flowrates (as measured with a bubble flowmeter) and the nominal peak of 498 nm is also shown for reference. The measured concentrations closely follow the shape of the Stolzenburg's transfer function, suggesting minimal broadening of the transfer function caused by instrumental imperfections [40].

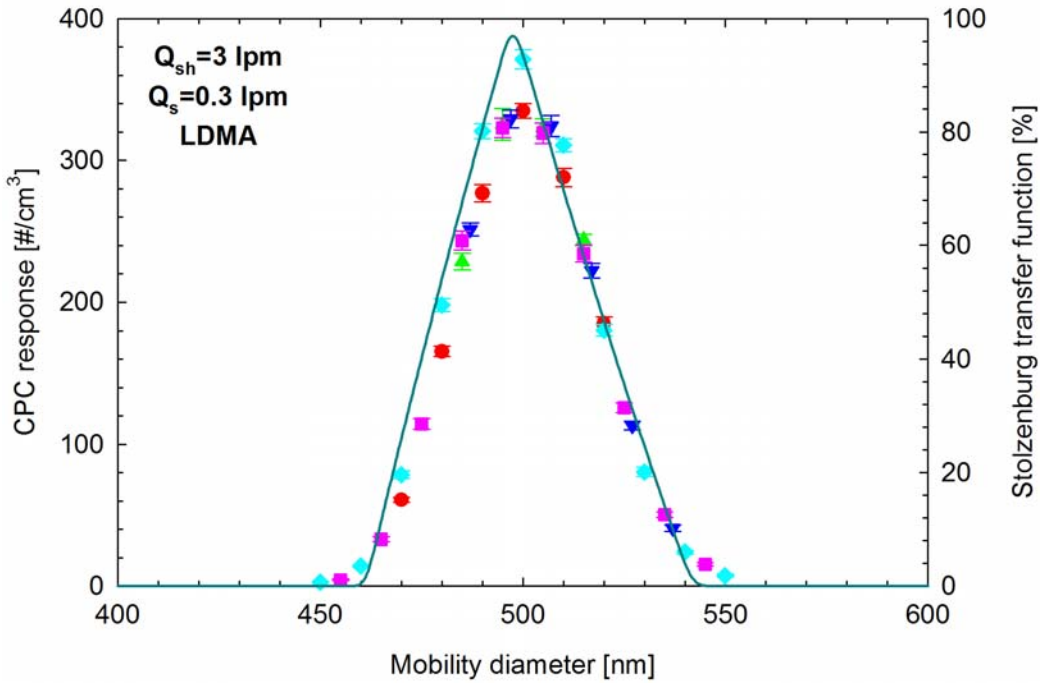

Figure 22: Measured concentrations of PSL spheres over step voltage changes of the LDMA center rod around the nominal PSL peak (dots). The error-bars indicate the variability in the number concentrations (expressed as one standard deviation) over the 60 s sampling time over each voltage setting. Also shown is Stolzenburg's transfer function (solid line) calculated at the nominal particle size of 498 nm.

Figure 23 shows measured number concentrations over step voltage changes of the Grimm-DMA around the nominal peak of the PSL spheres at sample flowrates of 0.3 lpm and 1 lpm. Also shown are Stolzenburg's transfer functions (eq. 28) calculated at two center rod lengths. All operating flowrates were measured with a bubble flowmeter, with the measured values suggesting balanced flows within a 4% accuracy. The best fit with the calculated Stolzenburg transfer functions was obtained assuming an effective center rod length of 41.5 cm rather than the nominal value of 44 cm, and was accordingly employed instead in the subsequent analysis.

It should be noted that the inlet impactor of the instrument was removed to allow operation of the DMA at sample flowrates of higher than 0.3 lpm without introducing a significant pressure drop. Additionally, some preliminary checks revealed a leakage resulting in a bimodal transfer function, which was resolved by means of wrapping some Teflon tape around the o-ring sealing the center rod at the base of the DMA. It is not clear to what extent these modifications have affected the effective length of the center rod. It needs to be stressed that the particular DMA is a very old design which was shortly replaced by Grimm by the Hauke type DMA.

.

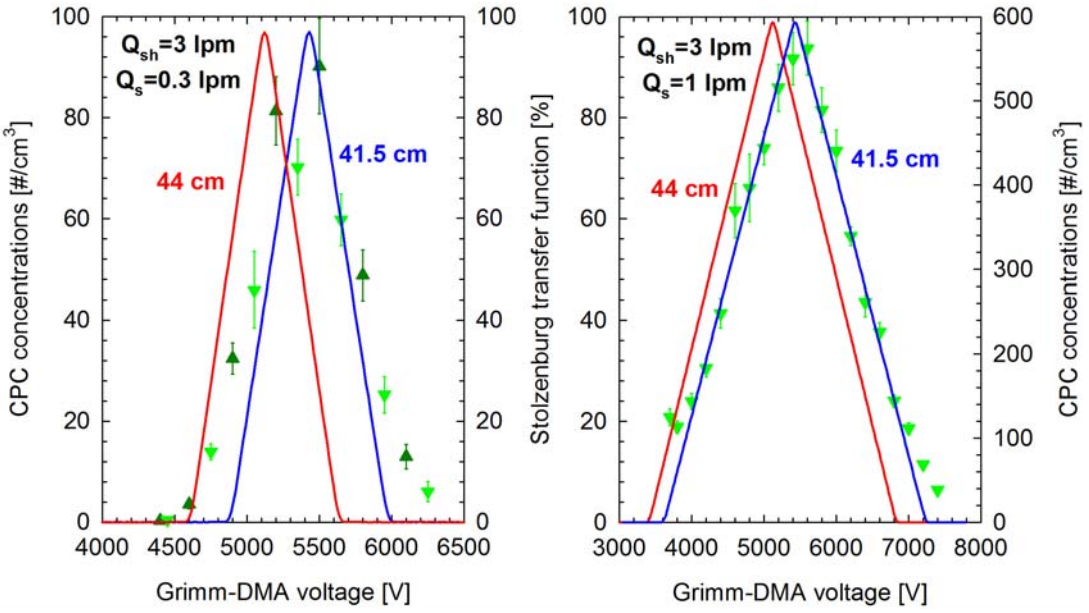

Figure 23: Measured concentrations of PSL spheres over step voltage changes of the Grimm-DMA center rod around the nominal PSL peak (dots) at sample flowrates of 0.3 lpm (left-hand panel) and 1 lpm (right-hand panel). The error-bars indicate the variability in the number concentrations (expressed as one standard deviation) over the 60 s sampling time over each voltage setting. Also shown is Stolzenburg's transfer function (solid line) calculated at the nominal particle size of 498 nm assuming a center rod length of 44 and 41.5 cm.

4.2 Calibration of the 3025A CPC

As stated in the experimental section, the TSI 3025A CPC was calibrated against silver nano-particles. Figure 24 shows the size distribution of the produced aerosol as measured with the TSI 3690N25 SMPS before the actual calibration experiments. Also shown are the fractions of singly and doubly charged particles assumed on the data inversion software [35]. Practically all particles in the size regime examined (sub 15 nm) were singly charged. In lack of a need to control the multiply charge fractions, a single DMA was employed. TSI Nano-DMA was selected in order to minimize particle losses at this small size range.

Figure 25 shows the experimentally determined detection efficiencies of the 3025A CPC measured against the 3068B electrometer (Figure 1). The generator produced very high concentrations of nano-sized particles as evident from the high electrometer responses (in excess of 40 fA in most of the tests at a sample flowrate of 1.5 lpm). The measured concentrations agreed within ±1 % (coefficient of variation) with the electrometer indications down to 5 nm, below which size the CPC reported lower concentrations in good agreement with the nominal detection efficiencies of the instrument.

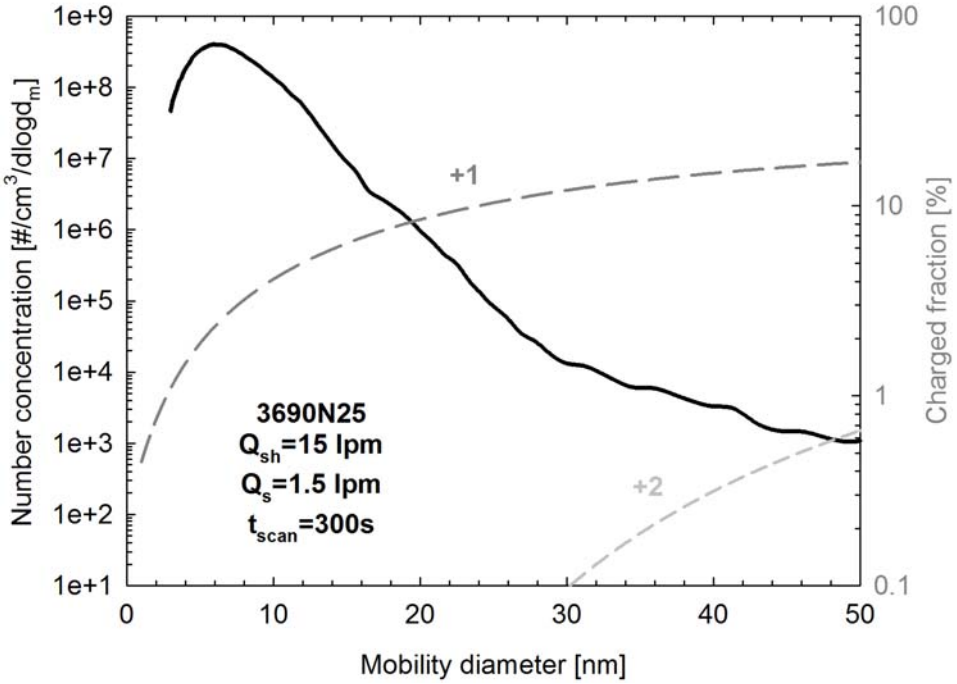

Figure 24: Measured size distribution of the silver particles produced in the SPG for the calibration of the TSI 3025A. The dashed lines illustrate the fraction of singly and doubly charged particles.

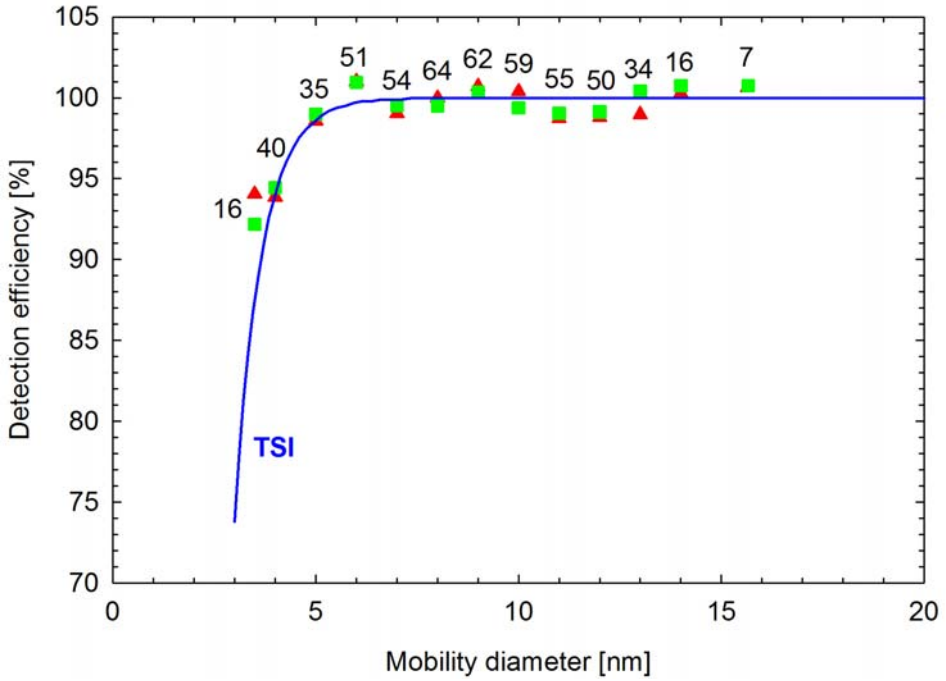

Figure 25: Experimentally determined detection efficiencies of the TSI 3025A CPC over two test sequences (illustrated with different symbols). The numbers on top of each measurement size corresponds to the average electrometer response at the two test sequences. Also shown is the nominal detection efficiency curve employed in the TSI SMPS data inversion algorithm.

4.3 Linearity measurements

4.3.1 Sample pressure effect

The 3068B electrometer monitors in real time the pressure at the inlet and the temperature at the (temperature-controlled) sensing zone and accordingly adjusts the volumetric flowrate to maintain the mass flowrate constant. Some dedicated measurements were performed in order to verify whether the flow adjustments were accurate. In these tests, a needle valve was installed at the inlet of the electrometer to control the inlet pressure and the sample flowrate was measured with a bubble flowmeter installed upstream of the needle valve (through a 20 cm long silicon tube). Figure 26 shows the measured volumetric flowrates as a function of the inlet pressure. The changes are in good agreement with the calculated volumetric flow change assuming that the mass flowrate is maintained at the set value of 1 slpm.

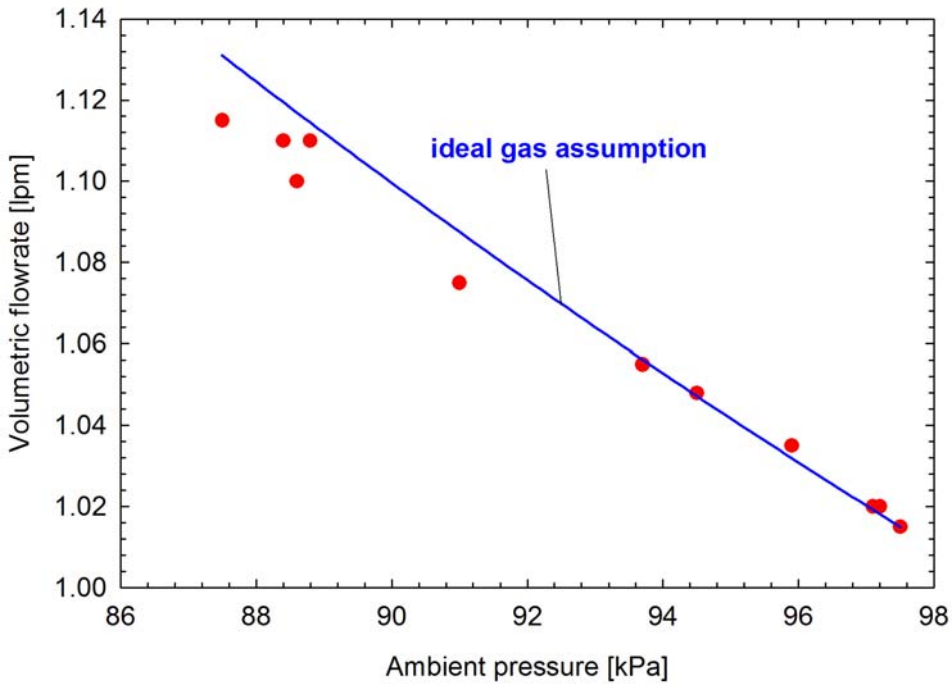

Figure 26: Volumetric sample flowrates (red dots) of the 3068B electrometer as measured with the bubble flowmeter at different inlet pressures measured with the pressure transducer located inside the electrometer. Also shown is the calculated ideal gas correction (blue line) assuming that the mass flowrate remains constant.

The flowrate of the 3790 and 3010 CPCs is controlled by a critical orifice that is maintained at constant temperature (optics temperature). Accordingly, the mass flowrate at the sample inlet is proportional to the inlet pressure and does not depend on the inlet temperature [41]. Actually, the pressure drop upstream of the critical orifice, which is also monitored, needs to be accounted for, even though this correction has a small effect [42]. In order to check the validity of this assumption some dedicated experiments were performed using the setup shown in Figure 3, modified to introduce a needle valve at the inlet of the 3790. Changes in the concentrations upstream of the needle valve (due to changes in the TDMA sample flows), were monitored with the 3025A CPC which was sampling in parallel, and were accounted for. The resulting changes in the 3790 concentration are plotted in Figure 27 as a function of the

measured inlet pressure. A clear decrease of the inlet concentration with decreasing inlet pressure was observed in good agreement with the expected mass flow rate reduction. The concentration changes were somehow higher, with the absolute difference increasing from less than 1% at 94 kPa to 4.5% at 86.7 kPa. This could be attributed to particle losses inside the needle valve which are expected to increase with increasing throttling and accordingly the under-pressure. It should be mentioned at this point that the under-pressure at the sampling point during the calibration experiments ranged between 3 and 5 kPa.

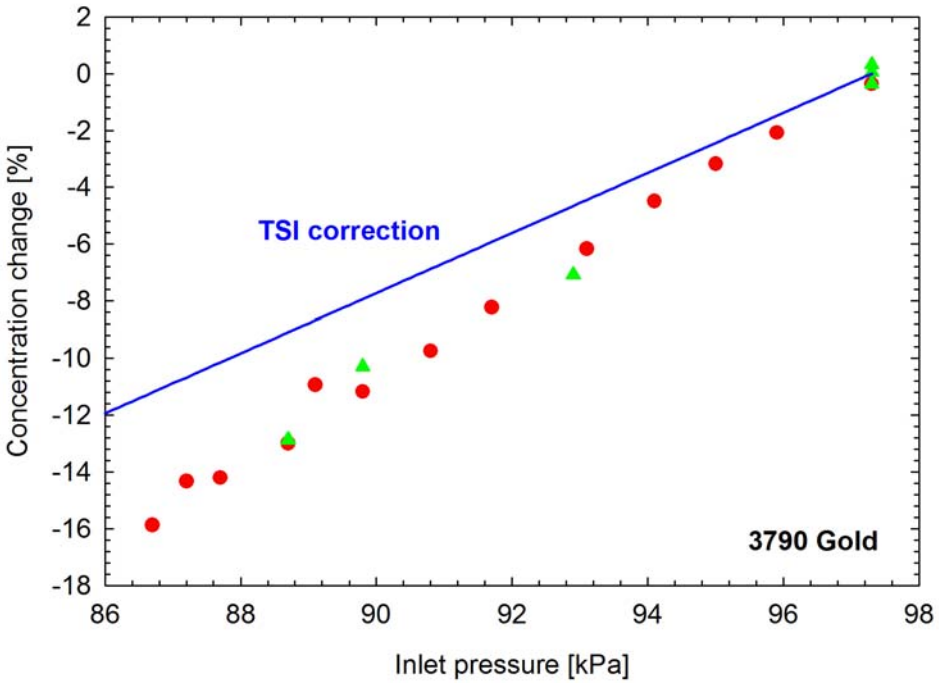

Figure 27: Changes in the measured concentrations of the 3790 CPC resulting from throttling of the 3790 inlet as a function of the inlet pressure. Also shown is the estimated concentration change resulting from the change of the mass flowrate caused by pressure changes.

The approach employed in the present study to account for the inlet pressure effect, was to measure the volumetric flowrate of both the electrometer and the 3790 CPC connected at the calibration configuration before and after each set of experiments. Since both instruments were exposed to the same inlet temperature and pressure, the mass flowrate should be proportional to the volumetric one. Accordingly the relative indications of the two instruments were corrected for the volumetric flowrate ratios. This assumption is not strictly valid in the case of temperature fluctuations for the 3790 but the overall effect is minimal since the ambient temperature remained within 21 to 28°C during the whole measurement campaign (maximum 1-(273.15+21)/(273.15+28)=2% error).

4.3.2 CPC spikes occurring during butanol filling

Sometimes during the zero level checks (see section 2.3.3) the 3790_Gold CPC gave some high concentration spikes which were not observed in the electrometer response.

Figure 28 illustrates the raw data from a test where the CPC gave three spikes (during three subsequent filling attempts) one of which peaked at 4800 #/cm^3 (equivalent to approximately 16 fA at the electrometer settings employed) when the electrometer remained at zero levels. It needs to be stressed that this was an extreme case, since usually the concentration spikes were smaller in magnitude (~100-300 #/cm^3). These spikes were found to coincide with butanol filling.

It is not clear whether these spikes are related to electrical noise caused by the opening of the butanol valve or over-dosing of butanol. The latter could potentially result in butanol droplets entering the saturator or even temporarily high supersaturations sufficient to initiate homogeneous nucleation of butanol vapours inside the condenser. It is worth noting that such behaviour was not observed in the other two 3790 models tested in the study. Whatever the origin of these false counts, they could explain the spikes observed in the measurements of Johnson et al. [43]. The raw data was checked for such spikes the presence of which constituted the data invalid.

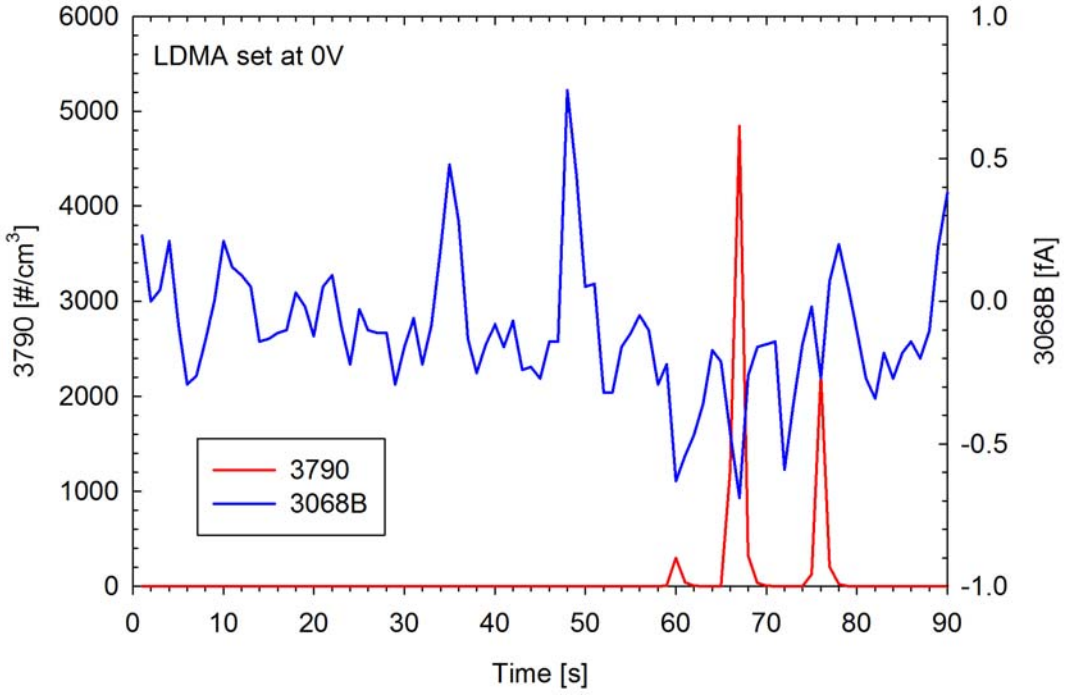

Figure 28: Typical concentration spike in the 3790_Gold response occurring during some of the zero level checks.

4.3.3 Linearity tests

Typical size distribution downstream of a TDMA setup exhibit distinct peaks corresponding to mainly singly or mainly doubly charged particles (and to a much lesser extend triply charged particles) as shown in Figure 18. Doubly charged particles produce double as much electrometer signal compared to singly charged particles for the same number concentration. Given that the major limitation of calibrating CPCs against electrometers is the relatively low electrometer sensitivity [7], the use of doubly charged particles has the potential to effectively half the lowest number concentration that can be calibrated against an electrometer.

In order to investigate this possibility, some dedicated experiments were performed, the results of which are summarized in Figure 29. The right-hand panel compares the measured TDMA response under an exponentially varying voltage of the second DMA (LDMA) to the simulated TDMA response following the analysis described in section 3.2. It should be noted that it was not possible to compare the absolute levels since the TDMA inlet concentrations were adjusted between the SMPS (used to simulate the TDMA responses - Figure 18) and the TDMA tests, using the dilution bridge (Figure 2).

While the simulated TDMA response captures the general shape of the measured TDMA response, the relative magnitude of the different peaks is not reproduced accurately. The two peaks at 65 and 98 nm correspond to doubly and singly charged particles of the same size, and therefore the deviations between the simulated and measured responses can not be attributed to diffusional losses or size-dependent counting efficiencies. The particles at the two larger peaks (98 nm and 142 nm) differ in size but at such large diameters diffusional losses and CPC counting efficiencies are not expected to have affected the relative counts. These findings (which were consistently observed during the whole measurement campaign) rather indicate that the charging probabilities may differ from those commonly assumed when inverting DMA data. This is in agreement with what the distributions of the resuspended PSL spheres suggest (Figure 21).

The simulated TDMA responses suggest that the average number of charges at the three peaks, namely 65, 98 and 142 nm, were 2.024, 1.034 and 1.005, respectively. These figures suggest that the peak at the largest size is the least affected by multiply charges and therefore should give the most accurate results for a given number concentration. The left-hand panel in Figure 29 summarizes the calibration results for this particular experiment. In the measurements, the TDMA inlet concentration was adjusted in order to maintain similar number concentration at each size examined. Four to five successive measurements were performed at each set point in the second DMA. Filled symbols show the calculated relative difference between the 3790 and the electrometer (3068B) concentrations assuming an integer number of charges (1 or 2, accordingly). The results at the largest peak corresponding to the set diameter of both DMAs (98 nm) gave the largest difference, which was -13.9% (±0.4%). A smaller difference of -12.4% (±0.3%) was obtained in the tests at 65 nm. The tests with 142 nm particles gave an even lower difference of -10.4% (±0.6%).

A better agreement was obtained when using the estimated average number of charges per particle (2.024 at 65 nm, 1.034 at 98 nm and 1.005 at 142 nm). The corresponding figures shown with open symbols in Figure 29, were -11.4% (±0.3%) at 65 nm, -11.0% (±0.5%) at 98 nm and -9.9% (±0.6%) at 142 nm. The somehow smaller differences at 142 nm may point towards higher counting efficiencies at this larger particle size even if the difference is statistically insignificant. Most probably though, the difference is related to uncertainties in the calculated number of charges, given the observed discrepancies between the simulated and measured TDMA responses.

In order to further increase the sensitivity of the electrometer, the possibility to use higher sample flowrates was also investigated. Dedicated tests were performed at electrometer sample flowrates of 1 lpm and 5 lpm. The TDMA inlet concentrations were step-wisely adjusted to achieve different electrometer levels, that spanned from 70 fA down to 10 fA. Two repetitions were performed at each concentration level.

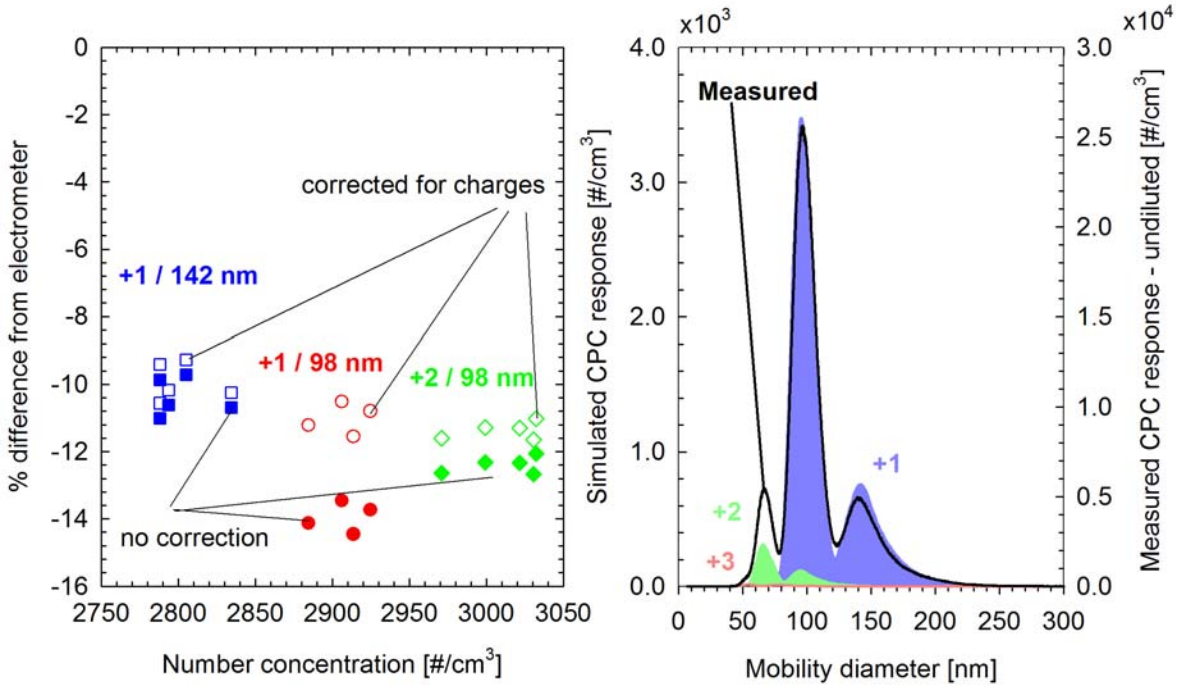

Figure 29: Counting efficiencies of the Golden 3790 CPC at 98 and 142 nm (left-hand panel) and the corresponding measured and simulated TDMA responses (right-hand panel). The "corrected" detection efficiencies (open symbols) were determined using the concentration weighted average charge suggested by the simulated TDMA responses.

The results of these experiments are summarized in Figure 30. The results obtained with singly charged (estimated average number of charges per particle was 1.022) 100 nm particles at an electrometer flowrate of 1 lpm, suggested an average difference of -12.5% (±0.5%) over the concentration range of 2300-12500 #/cm^3. The individual differences did not show any dependence on the concentration level examined, given the variability observed over the repetitions at a given concentration level. The results for doubly charged (estimated 2.005 charged per particle) 100 nm particles at an electrometer flowrate of 1 lpm suggested an average difference of -14% (±0.4%) over the concentration range of 1700 to 2700 #/cm^3. The corresponding figures for an electrometer flowrate of 5 lpm were -11.4% (±0.4%) for singly charged particles over the concentration range of 690 to 3100 #/cm^3 and -11.6% (±0.6%) for doubly charged particles over the concentration range of 320 to 630 #/cm^3.

Overall, the relative difference between the 3790 CPC and the electrometer concentrations remained within -10 to -14% over the number concentration range of 330 to 12000 #/cm^3. There appears to be a systematic yet statistically insignificant difference in the levels obtained at different electrometer flowrates of particle charge states probably originating from errors in the flowrate measurements and the estimation of the actual charge state.

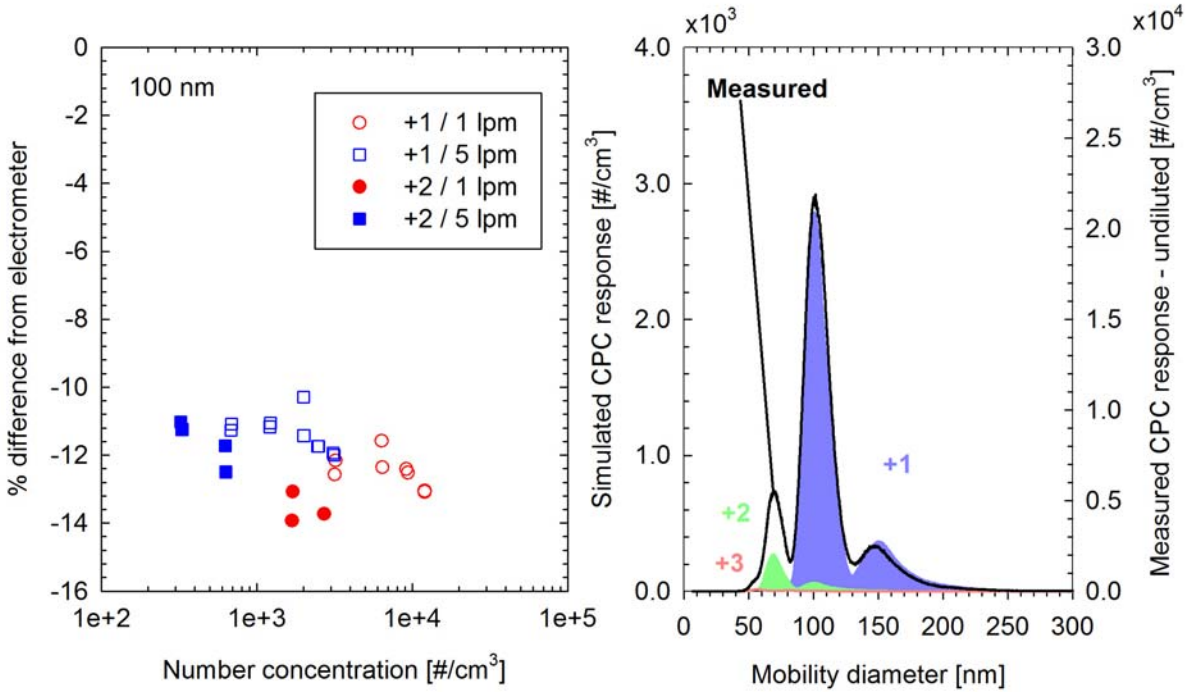

Figure 30: Counting efficiencies of the Golden 3790 CPC at 100 nm (left-hand panel) and the corresponding measured and simulated TDMA responses (right-hand panel). Different symbol colors correspond to different electrometer sample flowrates (red for 1 lpm and blue for 5 lpm). Open symbols indicate results obtained using singly charged particles at 100 nm while filled symbols correspond to results obtained using doubly charged particles.

4.4 Detection efficiencies

4.4.1 Pressure effect

The TSI 3025A CPC employed as the reference instrument for the characterization of the 3010 and 3790 detection efficiencies incorporates a complex flow scheme with three internal flow splittings. Accordingly, its operation is very sensitive to inlet pressure fluctuations. Yet it is difficult to predict the effect of inlet pressure on the recorded concentrations. In that respect, some dedicated experiments were performed in which the 3025A CPC was sampling in parallel to the 3790_Gold CPC, graphite particles classified in the LDMA (set at 115 nm). A needle valve was installed upstream of the LDMA to control the inlet pressure in both CPCs. The number concentration was maintained approximately constant at 3500 #/cm^3 during these tests.

The relative difference (using 3025A as a reference) between the two CPC indications are shown as a function of the inlet pressure (as determined with the 3790 CPC) in Figure 31. The results suggest a slightly different influence if the inlet pressure in the indications of the two CPCs. The relative difference in the concentrations changed from approximately -8% at 96 kPa to approximately -11% at 87 kPa. Over the range of inlet pressures encountered in the calibration experiments (92 to 95 kPa) the overall effect was less than 2% and was therefore disregarded from the subsequent analysis. In that respect, no pressure correction was employed in the indications of the two instruments. The volumetric sample flowrates were checked regularly though during the campaign with the bubble flowmeter and the day to day variations were found to be less than 2%.

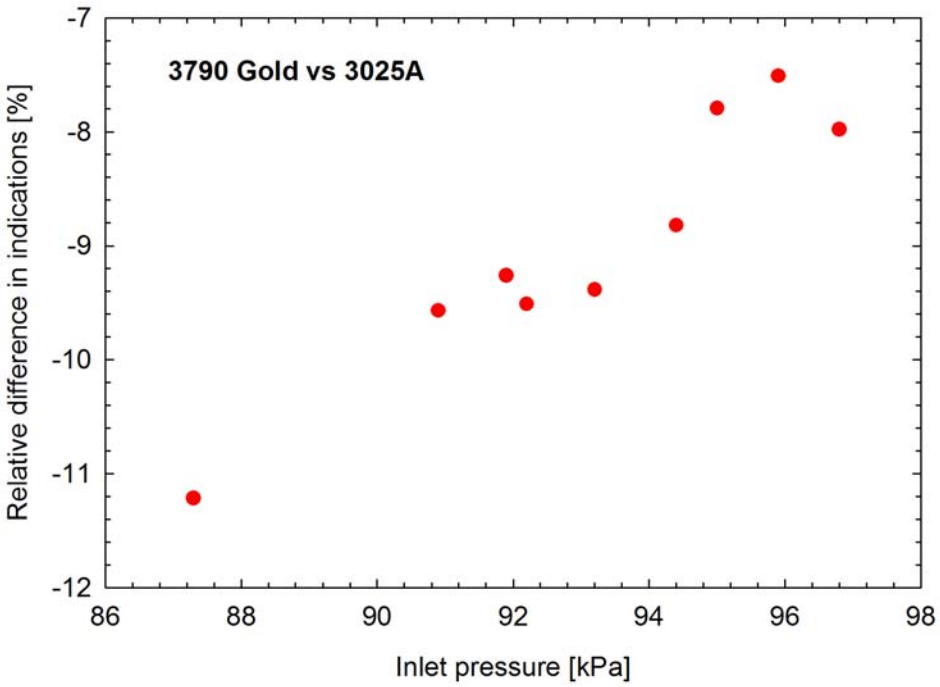

Figure 31: Relative difference between the indicated concentrations of the 3790_Gold and the 3025A CPCs at different inlet pressures. The calibration particles were graphite aggregates classified in the LDMA set at 115 nm.

4.4.2 CPC inter-comparisons

The linearity of the 3025A and the 3010 CPCs was not checked against the electrometer as the latter was available for a limited number of tests. Instead, some inter-comparisons were performed against the reference 3025A CPC. Figure 32 shows the results of these checks, which suggest that the relative difference for the different CPCs remained constant within ±1% over the concentration range of 150 to 8000 #/cm^3. The 3010 CPC gave very low particle counts, outside the specifications of the manufacturer. This performance degradation of the particular instrument was known and already reported in a previous study [44].

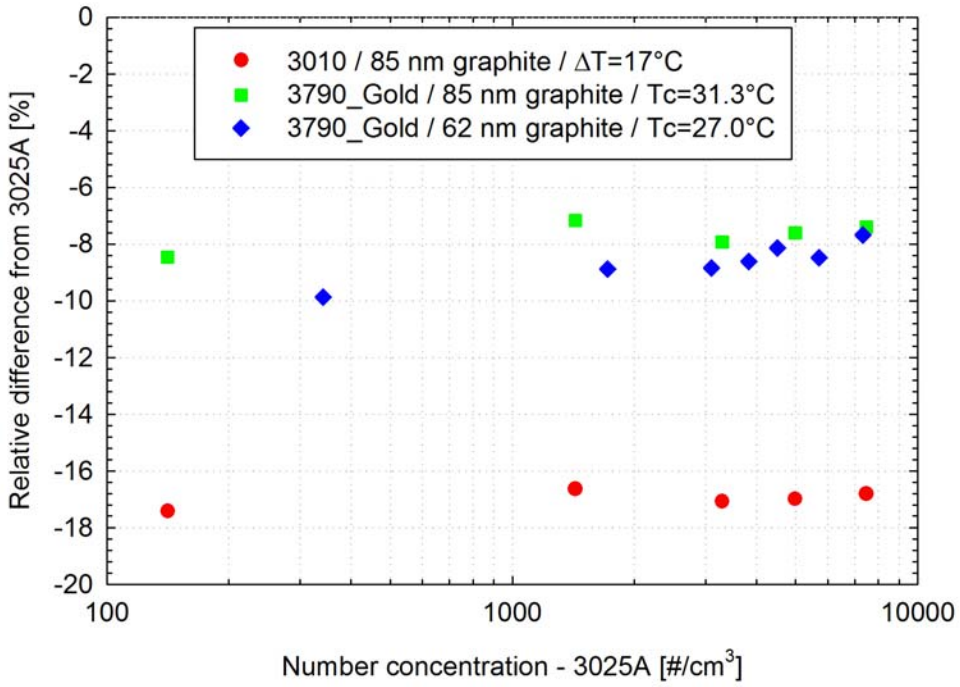

Figure 32: Cross-comparison of the 3010, 3790_Gold and 3025A CPC responses to monodisperse graphite particles at different concentration levels.

4.4.3 Counting efficiencies of the 3790_Gold CPC

Figure 33 summarizes the experimentally determined counting efficiencies of the 3790_Gold for PAO and graphite particles over a range of operating temperatures selected around the nominal values. The results were normalized with respect to the peak detection efficiency obtained over each measurement date (always PAO at elevated temperature difference – around 93%).

Focusing at the manufacturer set operating temperatures (31.7°C and 38.3°C), the counting efficiency for 23 nm PAO particles was found to be 49%, 51% and 54 % over the three test repetitions performed. These figures verify the calibration certificate of the instrument which was based on measurements with PAO. The counting efficiency for 23 nm graphite particles was only 34%, a figure that is outside the specifications laid down in the European regulation [2] (38-62%). The differences were more evident at larger sizes with the counting efficiency at 41 nm being 90 to 92% for PAO but only 77% for graphite, which again did not fulfil the regulatory requirements.

The differences in the counting efficiencies of PAO and graphite particles were more pronounced at low saturator-condenser temperature differences. This behaviour is consistent with what the heterogeneous nucleation model predicts for materials of different contact angles. For example, Figure 33 also shows the predicted counting efficiencies for contact angles of 0° and 10°. These two values were found to reproduce best the onset of the experimentally determined counting efficiencies at the lowest temperature difference examined. The numerical calculations predict that the 50% counting efficiency will differ by less than 1 nm at a 27°C / 38.3°C (condenser / saturator temperature) setting but more than 8 nm at a 32.7°C / 38.3°C. The experimentally determined shifts in the 50% counting efficiency were 0.6 nm at a 27°C / 38.3°C setting and 9.2 nm at a 32.7°C / 38.3°C in very

good agreement with the numerical calculations. Interestingly, the numerical calculations also predicted well the onset of particle activation at the different temperature settings examined. The absolute differences in the sub-50% portion of the counting efficiency curves were less than 6%, that is around the experimental uncertainty over the steep part of the curve.

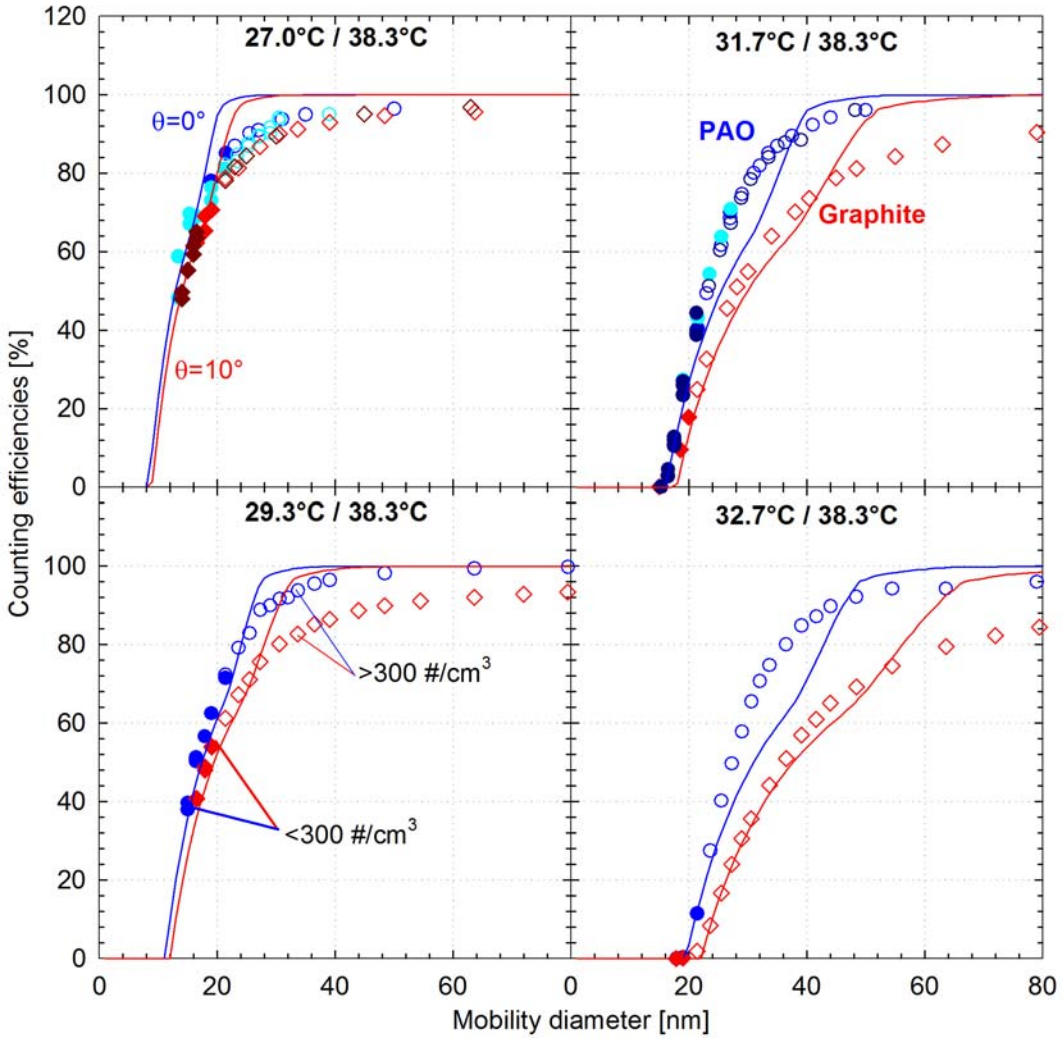

Figure 33: Experimentally determined counting efficiencies of the 3790_Gold CPC for PAO (blue symbols) and graphite (red symbols) particles at different operating temperatures. Tests conducted on different days are shown with different color shading. Open symbols indicate counting efficiencies determined at concentration levels higher than 300 #/cm^3 while filled symbols correspond to counting efficiencies determined at concentration levels of less than 300 #/cm^3. Also shown are the theoretically predicted counting efficiencies for contact angles of 0° (blue line) and 10° (red line).

The deviations from the model though were larger above the 50% counting efficiency, especially at the lowest temperature differences examined. The model yielded systematically higher counting efficiencies in the >80%-90% region. This range is strongly affected by the activation of particles near the condenser walls, where the critical saturation ratios occur within a very narrow range. Distortions in the flow and especially in the temperature profile at the inlet of the condenser were shown to have a very strong effect on the activation of the

particles in the wall (Figure 10 and Figure 12). It is therefore expected that temperature and flow non-idealities have contributed to this systematic underestimation.

One particular observed inconsistency relates to the very high counting efficiencies measured with PAO in the 50-80% range mostly evident at the two lowest temperature differences observed. The experimental data were found to lie above the maximum predicted counting efficiencies corresponding to perfectly wettable particles (under the assumptions of fully developed laminar flow and uniform temperature profile). Similar findings were observed by Giechaskiel et al. [6], who attributed this inconsistency in contamination of PAO particles due to incomplete evaporation of the buffer solution (50%-50% ethanol and isopropanol with 67 mM ammonium acetate) employed in the electrospray generator employed in their study. However, due to the generation method employed in the present study, contamination of the generated PAO particles is not considered likely. Temperature and flow non-idealities seem a more plausible reason for these discrepancies.

4.4.4 Counting efficiencies of the 3790_JRC CPC

Figure 34 summarizes the experimentally determined counting efficiencies of the 3790_JRC for PAO and graphite particles. Similar trends were observed, with the CPC exhibiting lower efficiency in detecting graphite particles than PAO. The difference was more evident as the operating temperature difference decreased.

The PAO results at the manufacturer's set temperatures of 31.3°C / 38.3°C (condenser / saturator temperature), suggested a counting efficiency at 23 nm of 48% and 50% over the two test repetitions, verifying the calibration certificate of the instrument, obtained with emery oil. It is interesting though to note that the 3790_JRC CPC is set at a 0.4°C higher temperature difference in order to achieve the same 50% counting efficiency with the 3790_Gold CPC. Similar and even larger differences (up to 0.9°C) in the set temperature differences of 3790 CPCs have been reported by Giechaskiel et al. [5].

Such variation in the temperature settings probably reflect manufacturing imperfections, but constitute modelling of the CPC performance challenging especially considering the generally low operating temperature differences (nominal 6.6°C). For example Figure 35, compares the experimentally determined counting efficiencies of the two 3790 CPCs at their nominal operating temperatures for PAO particles with numerical calculations for perfectly wettable particles over the range of temperature differences reported by Giechaskiel et al. [5]. The experimental data are in very good agreement despite the 0.4°C difference in the set temperature difference. Yet the numerical model suggests that this 0.4°C difference can result in a shift of the counting efficiencies by 5% to 10% over the steep part of the curve. The extended range of operating temperature differences reported by Giechaskiel et al. [5] would result in a shift of 12% to 21%. Any modelling results therefore need to be assessed taking such uncertainties into consideration.

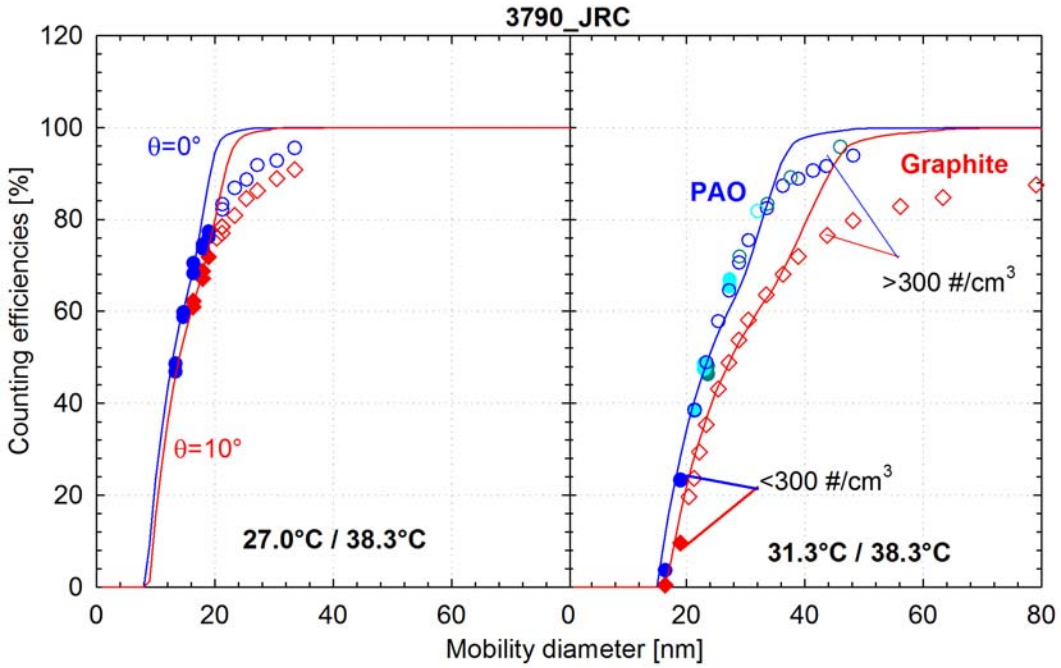

Figure 34: Experimentally determined counting efficiencies of the 3790_JRC CPC for PAO (blue symbols) and graphite (red symbols) particles at different operating temperatures. Tests conducted on different days are shown with different color shading. Open symbols indicate counting efficiencies determined at concentration levels higher than 300 #/cm^3 while filled symbols correspond to counting efficiencies determined at concentration levels of less than 300 #/cm^3. Also shown are the theoretically predicted counting efficiencies for contact angles of 0° (blue line) and 10° (red line).

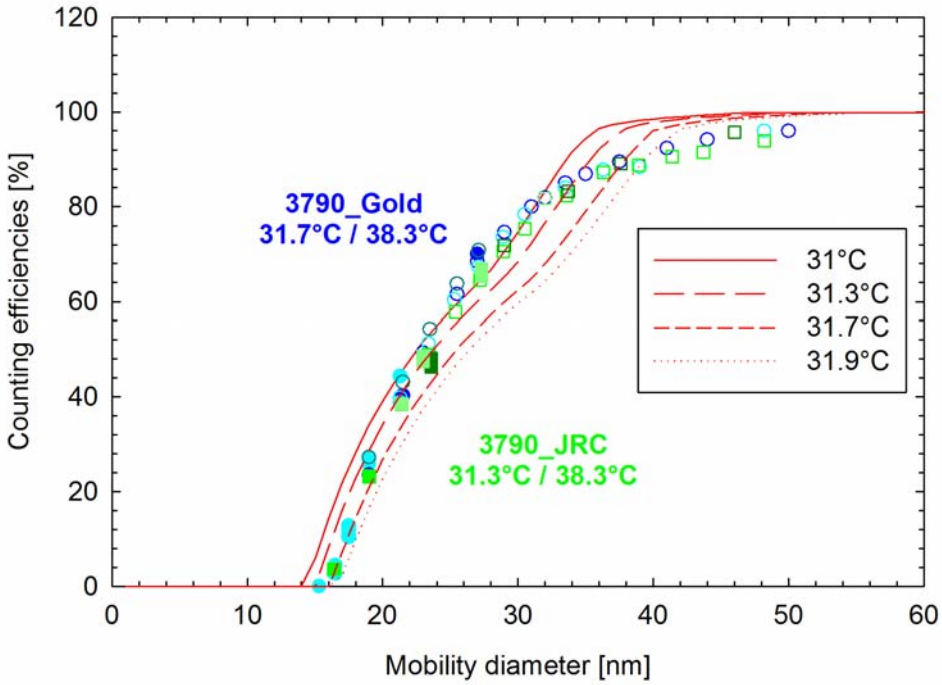

Figure 35: Comparison of experimentally determined counting efficiencies of the two 3790 CPCs tested in the study at their nominal operating temperatures for PAO with numerical calculations for perfectly wettable particles over the range of set condenser wall temperatures reported for 3790 CPCs [5].

4.4.5 Effect of the operating temperatures on the peak detection efficiencies of the 3790 CPC

The use of the 3025A CPC as a reference instrument introduced some uncertainty in the calculation of the 3790 absolute detection efficiencies due to the complex flow scheme and the associated uncertainties introduced by the day to day variation in inlet pressures (e.g. Figure 31). To account for this, the indications of the CPC under calibration were checked regularly against the 3025 at a size large enough to ensure a 100% counting efficiency (typically 100 or 160 nm). These checks were performed following each change of the operating temperature or calibration particle material.

A common observation during these checks was that the peak counting efficiencies depended on the operating temperature difference of the 3790. One particular measurement day consisted of a sequence of tests with graphite at different condenser temperatures of the 3790_Gold CPC, followed by tests PAO at some of the previously tested operating temperatures. The saturator temperature was held at 38.3°C during all these tests. The experimentally determined counting efficiencies at 160 nm are summarized in Figure 36, which suggests a clear dependence on the temperature difference and the calibration particle employed. Higher counting efficiencies were observed for PAO, ranging from 96% at a condenser temperature of 29.3°C to 93% at a condenser temperature of 32.7°. The counting efficiencies for graphite particles ranged from 92% at 27.3°C and 91% at 29.3°C to 83% at 32.7°C.

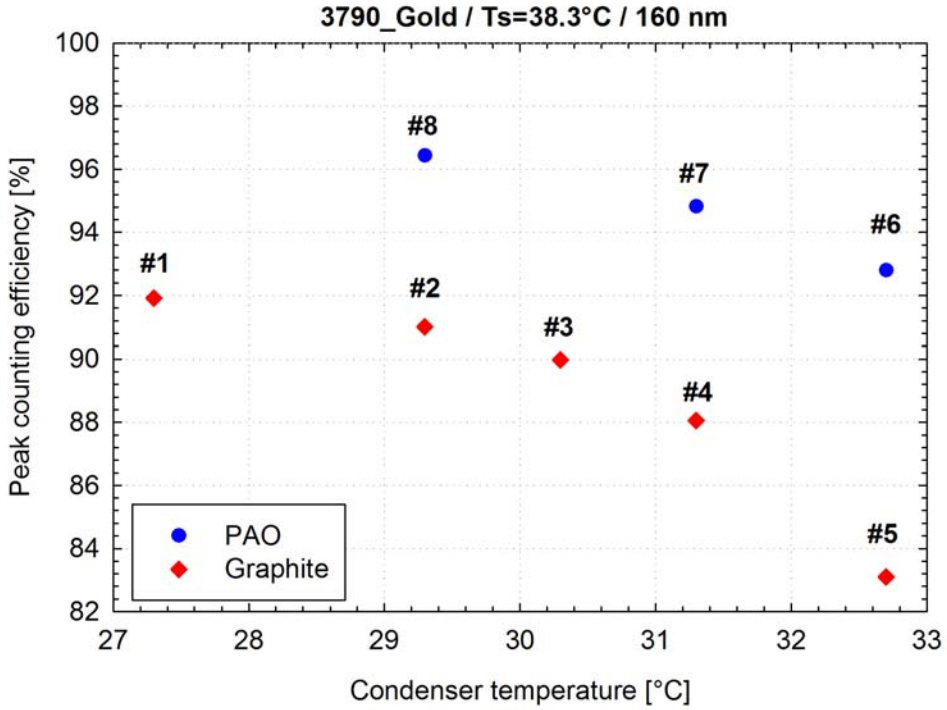

Figure 36: Peak counting efficiencies (uncorrected for the slope of the 3790) of the 3790_Gold CPC for 160 nm graphite (red dots) and PAO (blue dots) particles at different condenser temperatures. The numbers on top of each dot indicate the test sequence.

Similar trends were observed in some dedicated experiments with the 3790_JRC CPC. During these tests, the condenser temperature of the 3790_JRC was changed while sampling in parallel to the 3025A CPC monodisperse PAO particles (Figure 3) of 105 and 160 nm. The CPC was allowed to stabilize at each new temperature setting for at least 5 min during these tests, but it is recognized that longer stabilization times might be required. The results of these experiments are summarized in Figure 37. Similar trends were observed even if the absolute levels were different for the two CPCs. More specifically, a shift of the condenser temperature from 31°C and 31.3°C to 32.7°C resulted in a drop of the counting efficiency of both 105 nm and 160 nm particles from approximately 90% to around 85%.

This behavior is indicative of inefficient activation near the walls of the condenser. The calculated saturation ratio profiles (Figure 4) suggest that particle activation near the walls of the condenser occurs very close at the inlet. However, this region is difficult to accurately model due to the discontinuity in the temperature profiles (the wall being at the condenser temperature while the aerosol stream at the saturator temperature). The simplified calculations performed assuming a non-uniform inlet temperature profile (Figure 10) are in line with this observation. Still the heterogeneous nucleation theory can explain the different peak detection efficiencies for graphite and PAO.

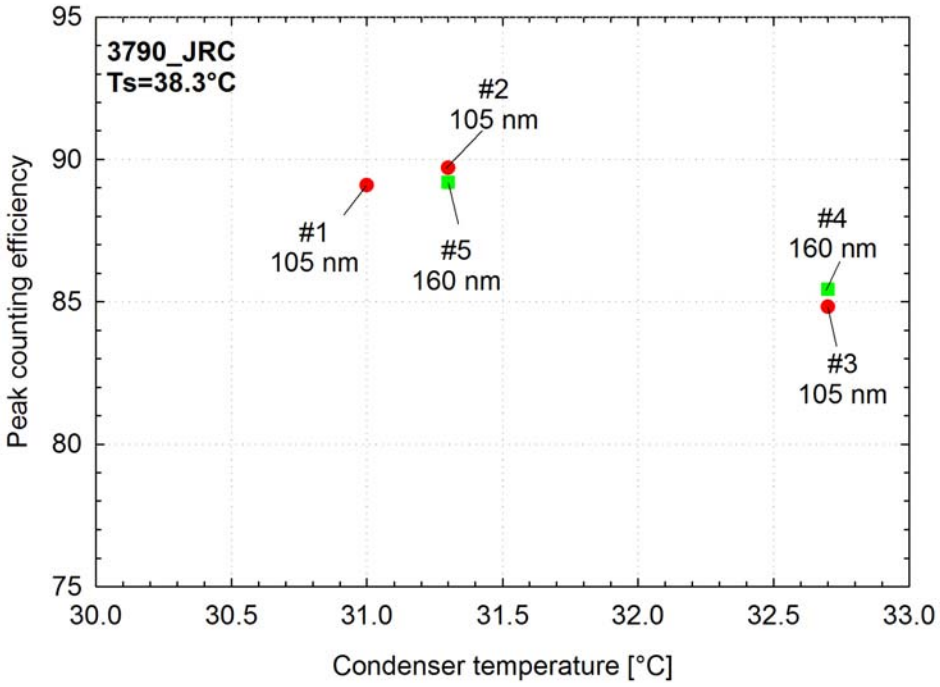

Figure 37: Peak counting efficiencies (uncorrected for the slope of the 3790) of the 3790_JRC CPC at 105 and 160 nm PAO particles as a function of the condenser temperature (saturator temperature always set at 38.3°C). The numbers illustrate the test sequence.

4.4.6 Counting efficiencies of the 3010 CPC

Figure 38 summarizes the experimentally determined counting efficiencies of the 3010 CPC for PAO and graphite particles at different temperature differences. As in the case of the 3790 CPCs, the instrument exhibited lower efficiency in counting graphite particles compared to PAO, with the relative differences increasing as the operating saturator-condenser temperature difference decreased.

The peak counting efficiencies were also found to depend on the calibration particle material and the operating temperature. More specifically, the peak counting efficiencies of 160 nm PAO particles (uncorrected for the level differences between the 3010 and the 3025A) increased from approximately 74% at a temperature difference of 6.6°C to ~81% at 11.3° and 14°C. The corresponding figures for graphite ranged from 71% at 6.6°C to 76% at 11.3°C and 14°C.

It was not possible to numerically calculate the counting efficiencies of the 3010 CPC since the geometry of the condenser is not known. The fact that similar trends were observed in the responses of the 3010 and 3790 CPC reinforces the observation that the material and temperature dependence observed reflect true differences in the activation of graphite and PAO particles.

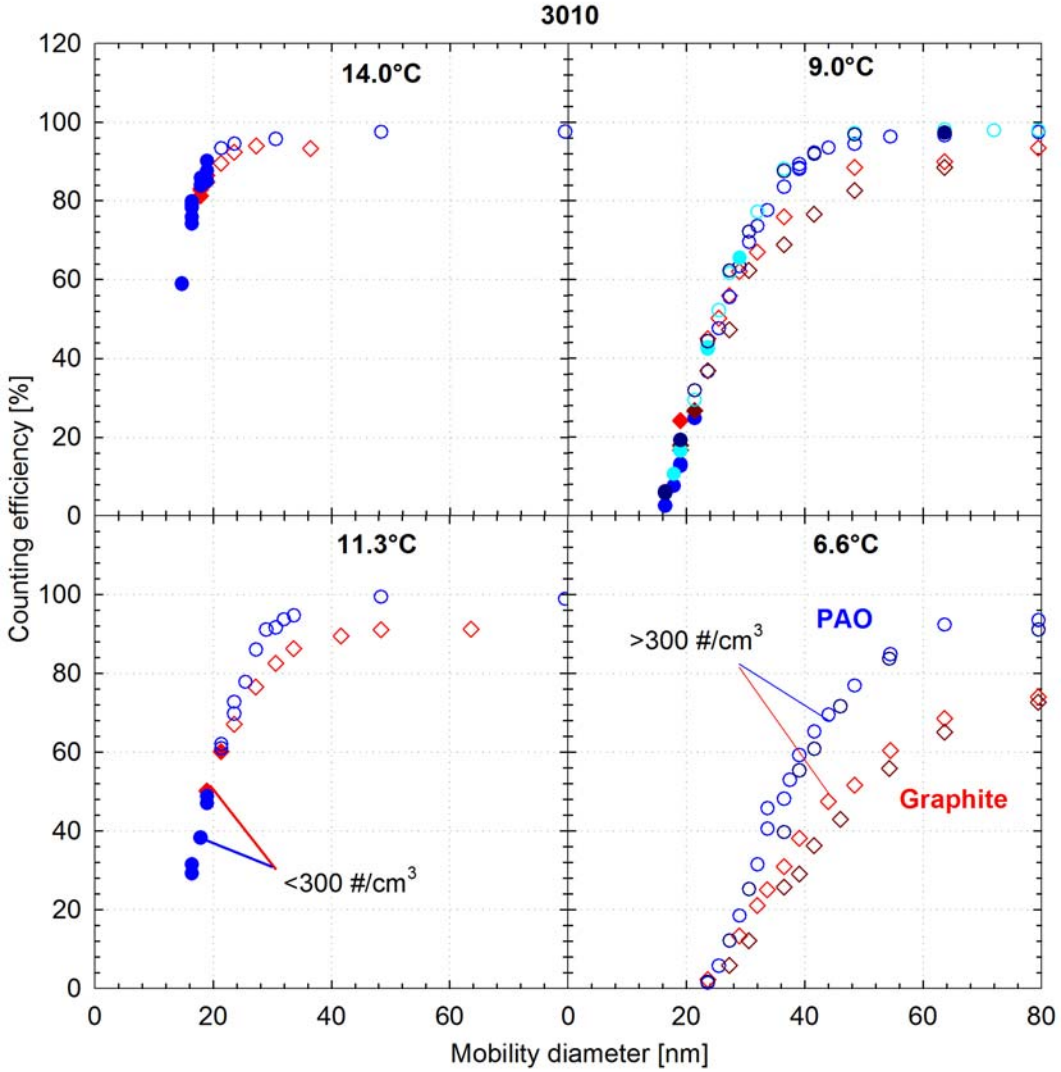

Figure 38: Experimentally determined counting efficiencies of the 3010 CPC for PAO (blue symbols) and graphite (red symbols) particles at different operating temperature differences. Tests conducted on different days are shown with different color shading. Open symbols indicate counting efficiencies determined at concentration levels higher than 300 #/cm^3 while filled symbols correspond to counting efficiencies determined at concentration levels of less than 300 #/cm^3.

4.4.7 Counting efficiencies for C14,C16 and C40

The 3790_JRC CPC was also tested against C14, C16 and C40 particles. Figure 39 compares the experimentally determined counting efficiencies for these thee alkanes against those determined with PAO. The lowest alkanes examined (C14 and C16) exhibited similar counting efficiencies with PAO, with differences lying within the experimental uncertainty of the measurements. The counting efficiencies were best reproduced assuming a contact angle of 0°, suggesting that all three materials behave as perfectly wettable particle seeds.

On the other hand, tetracontane particles (C40) resulted in very low counting efficiencies, best reproduced by contact angles in the 18 to 22° range. Similar, low counting efficiencies for C40 were observed by Giechaskiel et al. [4] when employing the same generator. Deposits forming on the impactor of the TDMA system and the generator suggested that the produced C40 particles were solid in nature, resembling paraffin wax.

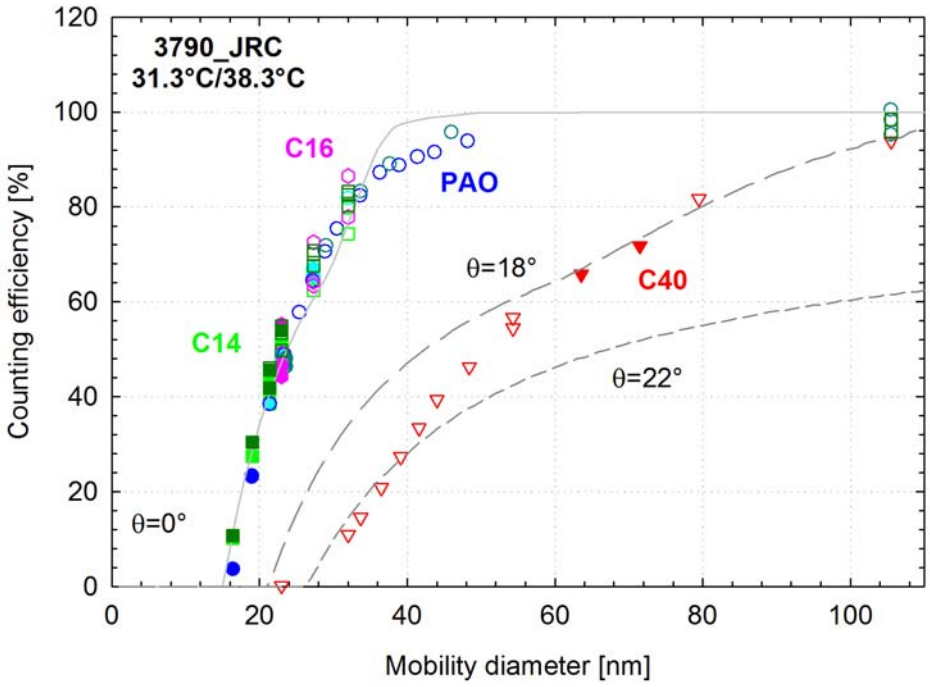

Figure 39: Experimentally determined counting efficiencies of the 3790_JRC CPC for PAO (blue symbols), C14 (green symbols), C16 (purple symbols) and C40 (red symbols) particles at the nominal operating temperatures of the instrument. Tests conducted on different days are shown with different color shading. Open symbols indicate counting efficiencies determined at concentration levels higher than 300 #/cm^3 while filled symbols correspond to counting efficiencies determined at concentration levels of less than 300 #/cm^3. Figure also illustrates the numerically calculated counting efficiencies for contact angles of 0°, 18° and 22°.

Interestingly, the deposits forming on the generator were found to affect subsequent calibration experiments with other materials even after long-run operation of the generator at elevated temperatures using nitrogen to purge the deposits. This is clearly illustrated in Figure 40 comparing experimentally determined counting efficiencies of the 3790_Gold with PAO particle before and after the tests with C40. The experimental data collected after the C40 test were accordingly disregarded from any further analysis.

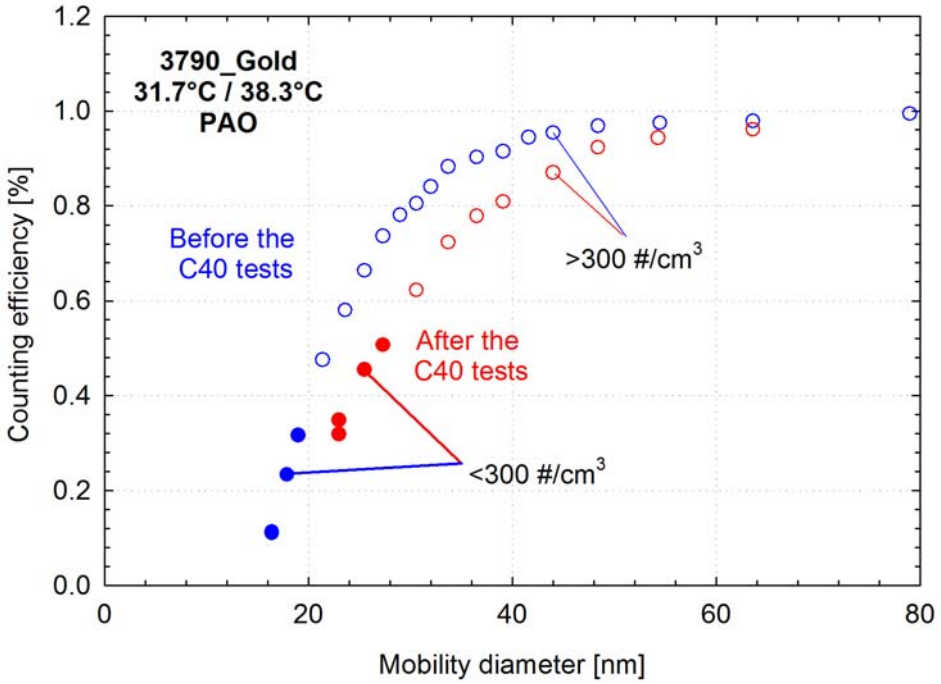

Figure 40: Experimentally determined counting efficiencies of the 3790_Gold CPC against PAO particles, before (blue symbols) and after (red symbols) the tests with C40.

4.4.8 Effect of particle charge state

In order to investigate any potential effect of the particle charge state on the experimentally determined counting efficiencies, a 1 mCi ^{85}Kr neutralizer was installed downstream the TDMA during some of the 3790_JRC tests with C14. The results of these investigations are summarized in Figure 41. No effect of the charging state could be identified in the measured counting efficiencies at 23 and 27.3 nm. The estimated fractions of charged particles at these two sizes after neutralization (Figure 19) are 22% and 27%, respectively, (practically all of them carrying a single positive or negative charge). The results verify the numerical calculations presented in Figure 13, suggesting that particle charges do not affect the critical saturation ratios for particle diameters larger than 10 nm.

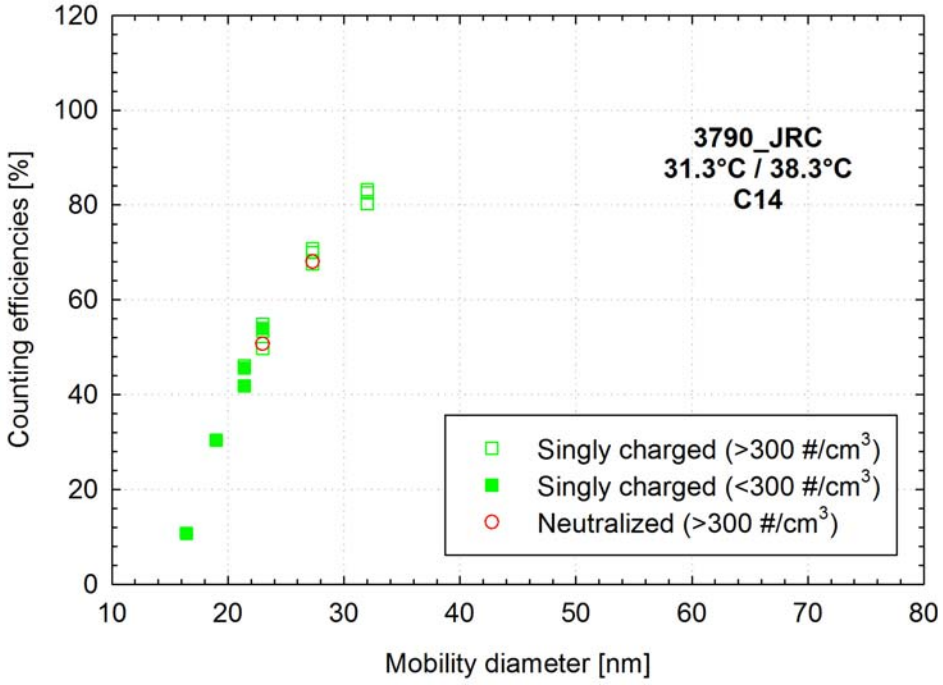

Figure 41: Experimentally counting efficiencies of the 3790_JRC CPC running at its nominal operating temperatures, against singly charged (green dots) and neutralized (red dots) C14 particles.

5 CONCLUSIONS

The present study investigated the effect of calibration material type on the counting efficiencies of PMP compliant CPCs as well as possibilities to check the linearity of the CPCs against electrometer in the sub 2000 #/cm^3 concentration range. The study focused on the TSI 3790 CPC but some measurements were also performed on a TSI 3010 CPC operating at reduced saturator-condenser temperature difference.

Two approaches were investigated in order to improve the sensitivity of the electrometer, namely a) the use of multiply charged particles of well defined charge state (employing a TDMA setup) and b) the operation of the electrometer at higher sample flowrates. Use of double charged particles and an electrometer sample flowrate of 5 lpm effectively resulted in a tenfold increase of the electrometer signal at a given particle number concentration level. Application of this methodology to a 3790 CPC yielded a 10% to 14% agreement with electrometer responses to 100 nm graphite particles across the particle number concentration range of 330 to 12000 #/cm^3.

Some small but systematic differences were observed between the results for singly and doubly charged particles suggesting inaccuracies in the small corrections for the charge status of the calibration particles. In a similar manner, simulated TDMA responses were found to capture the general shape of the measured TDMA signals but failed to reproduce the relative contribution of the different spikes (i.e. different charges). It is not clear whether and to what extent such discrepancies are related to the complex structure of graphite aggregates [45]. Size distribution measurements of nebulized spherical PSL particles revealed that the multiple-charge correction feature of the SMPS inversion algorithm fails to completely remove the PSL spikes from the background size distribution. These results provide evidence of inaccuracies in the characterization of the particle charge state even for spherical particles. Humidity or impurities in the air were shown to affect the size and mobility of ions produced inside a neutralizer, and could affect to a certain extent particle charging (e.g. [46] and references within it). This issue requires further investigation as it may have a strong effect on the accuracy of the calibration results, especially when a single DMA is employed for size classification [47].

The counting efficiencies of the CPCs were found to depend strongly on the material type of the calibration particles employed. The highest counting efficiencies for the 3790 CPCs were obtained for PAO, C14 and C16 particles, which furthermore were in very good agreement with the manufacturer's certificates at 23 nm and 41 nm. Graphite particles gave systematically lower counting efficiencies, even falling below the minimum allowed efficiencies at both 23 nm (38%) and 41 nm (90%) specified in the regulations. Limited tests with C40 particles resulted in even lower counting efficiencies with the CPC reaching a 50% counting efficiency at 50 nm.

The material type dependence of the counting efficiencies was found to decrease with increasing the operating temperature difference, this applying to both the 3010 and the 3790 CPCs. Numerical calculations assuming heterogeneous nucleation of butanol onto particle seeds also suggest that the importance of particle material (through the concept of the contact angle) becomes more important with decreasing temperature differences.

Comparison of the numerical calculations and the experimental data suggest a contact angle of 0° for PAO, C14 and C16 (perfectly wettable material), approximately 10° for graphite and 18-22° for C40 particles. In the calculation of these figures, the effect of line tension and curvature-dependence of surface tension (Tolman's length) were neglected.

Inclusion of such effects in the heterogeneous nucleation model had a profound effect on the calculated counting efficiencies. However the uncertainty associated with both the absolute levels and the signs of line tension and Tolman's length is too high that actually overwhelms the observed systematic differences in the counting efficiencies of PAO and graphite. Any modelling attempts are also subject to large uncertainties introduced by instrumental imperfections. Differences of up to 0.9°C were reported in the set operating temperature differences of CPCs of the same model to achieve the same counting efficiency. Some numerical calculations also showed that flow and temperature non-idealities can have a significant effect on the counting efficiencies of the instrument.

Some calculations on condensational growth of activated particles suggested that the latter grow to sizes larger than 4 um at the exit of the condenser and that growth happens within a few ms. Butanol depletion and temperature drop in the vicinity of an activate particle can reduce the local saturation ratio by up to 4 and 10%, respectively. However, it is unlikely that such reduction in the local saturation ratio would affect activation of neighbouring particles due to relatively large distance between particles (of the order of 0.5 mm at a concentration of 10000 #/cm^3).

The experimental data also provided evidence that the peak counting efficiency of the 3790 CPC, depends on the operating temperature difference and the calibration material. Changing the temperature difference from 11°C to 5.6°C reduced the peak counting efficiency of graphite particles from 92% to 83%. A decrease of the temperature difference from 10°C to 5.6°C reduced the peak counting efficiency from 96% to 93%. These results suggest insufficient activation of particles near the walls of the condenser.

6 LIST OF SPECIAL TERMS AND ABBREVIATIONS

CPC	Condensation Particle Counter
CVS	Constant Volume Sampler
DMA	Differential Mobility Analyzer
HEPA	High Efficiency Particulate Air
HDE	Heavy Duty Engine
LDMA	Long DMA (TSI's 3081)
MFC	Mass Flow Controller
PMP	Particle Measurement Programme
SMPS	Scanning Mobility Particle Sizer
TDMA	Tandem Differential Mobility Analyzer
VPR	Volatile Particle Remover

REFERENCES

1 Commission Regulation (EC) No 692/2008 of 18 July 2008 implementing and amending Regulation (EC) No 715/2007 of the European Parliament and of the Council on type-approval of motor vehicles with respect to emissions from light passenger and commercial vehicles (Euro 5 and Euro 6) and on access to vehicle repair and maintenance information. http://eur-lex.europa.eu/LexUriServ/LexUriServ.do?uri=OJ:L:2008:199:0001:0136:EN:PDF

2 Regulation No 83 of the Economic Commission for Europe of the United Nations (UN/ECE) – Uniform provisions concerning the approval of vehicles with regard to the emission of pollutants according to engine fuel requirements. http://www.unece.org/fileadmin/DAM/trans/main/wp29/wp29regs/r083r4e.pdf

3 Commission Regulation (EC) No 595/2009 of the European Parliament and of the Council of 18 June 2009 on type-approval of motor vehicles and engines with respect to emissions from heavy duty vehicles (Euro VI) and on access to vehicle repair and maintenance information and amending Regulation (EC) No 715/2007 and Directive 2007/46/EC and repealing Directives 80/1269/EEC, 2005/55/EC and 2005/78/EC. Available at: http://eur-lex.europa.eu/LexUriServ/LexUriServ.do?uri=OJ:L:2009:188:0001:0013:EN:PDF

4 Giechaskiel B., Wang X., Horn H.-G., Spielvogel J., Gerhart C., Southgate J., Jing L., Kasper M., Drossinos Y. and Krasenbrink A. (2009). Calibration of Condensation Particle Counters for Legislated Vehicle Number Emission Measurements. Aerosol Science and Technology, 43:1164–1173.

5 Giechaskiel B. and Bergmann A. (2011). Validation of 14 Used, Re-calibrated and New TSI 3790 Condensation Particle Counters According to the UN-ECE Regulation 83. Journal of Aerosol Science, 42: 195-203.

6 Giechaskiel B., Wang X., Gilliland D. and Drossinos Y. (2011). The Effect of Particle Chemical Composition on the Activation Probability in butanol Condensation Particle Counters. Journal of Aerosol Science, 42: 20-37.

7 Fletcher R. A., Mulholland G. W., Winchester M. R., King, R. I. and Klinedinst D. B. (2009). Calibration of a Condensation Particle Counter Using a NIST Traceable Method. Aerosol Science and Technology, 43: 425-441.

8 TSI (2010). Model 3010 Condensation Particle Counter. Instruction Manual. P/N 1933010, Revision F.

9 Mamakos A., Carriero M., Bonnel P., Demircioglu H., Douglas K., Alessandrini S., Forni F., Montigny F., Leseuer D. (2011). EU-PEMS PM Evaluation Program - Third Report – Further Study on Post DPF PM/PN Emissions. JRC Scientific and Technical Reports, EUR 24883 EN.

10 Gotoh A., Ikazaki H. and Kawamura M. (1990). Simple Generator of Ultrafine Particles for Tests. Journal of Colloid and Interface Science, 140:535-537.

11 Mamakos A., Ntziachristos L. and Samaras Z. (2008). Differential Mobility Analyser Transfer Functions in Scanning Mode. Journal of Aerosol Science, 39:227-243.

12 Russell, L., Flagan R. and Seinfeld J. (1995). Asymmetric Instrument Response Resulting from Mixing Effects in Accelerated DMA-CPC Measurements. Aerosol Science and Technology, 23:491-509.

13 Housiadas C., Ezquerra Larrodé, F. and Drossinos Y. (1999). Numerical Evaluation of the Graetz series. International Journal of Heat and Mass Transfer, 42: 3013-3017.

14 Fletcher N.H. (1958). Size Effect in Heterogeneous Nucleation. Journal of Chemical Physics, 29: 572-576.

15 Perry H. R., Green D. W. and Maloney J. O. (1999). Perry's Chemical engineers' Handbook. Seventh Edition. McGraw Hill, New York

16 Dean J. A. (1999). Lange's Handbook of Chemistry. Fifteenth Edition, McGraw Hill, New York.

17 Gibbs J.W. (1928) Collected Works. Vol 1. Thermodynamics, Longmans-Green, New York.

18 Tolman R.C. (1949). The Effect of Droplet Size on Surface Tension. Journal of Chemical Physics, 17:333-338.

19 Kaschiev D. (2000). Nucleation. Basic Theory with Applications. Butterworth-Heinemann publications. ISBN 0 7506 4682 9.

20 Scheibel H.G. and Porstendörfer J. (1985). Counting Efficiency and Detection Limit of Condensation Nuclei Counters for Submicrometer Aerosols. I-Theoretical Evaluation of the Influence of Heterogeneous Nucleation and Wall Losses. Journal of Colloid and Interface Science, 106: 261-274.

21 Lazaridis M. (1993). The Effects of Surface Diffusion and Line Tension on the Mechanism of Heterogeneous Nucleation. Journal of Colloid and Interface Science, 155: 386-391.

22 Scheludko A., Chakarov V. and Toshev B. (1980). Water Condensation on Hexadecane and Linear Tension. Journal of Colloid and Interface Science, 82:83-92.

23 Housiadas C., Ezquerra Larrodé, F. and Drossinos Y. (2000). Convective Diffusion in a Tube with Non-Uniform Inlet Conditions. Journal of Aerosol Science, 31: 959-968.

24 Wilson C.T.R. (1927). On the Cloud Method of Making Visible Ions and the Tracks of Ionizing Particles. In Nobel Lecture Physics. Elsevier, New York. !965.

25 Thompson J.J. (1967). Conduction of Electricity through Gases. Dover, New York.

26 Friedlander S.K. (2000). Smoke, Dust, and Haze. Fundamentals of Aerosol Dynamics. Second Edition. Oxford University Press, New York. ISBN 0-19-512999-7

27 Camero-Castano M., de la Mora J.F. (2002). Ion-induced Nucleation: Measurement of the Effect of Embryo's Size and Charge State on the Critical Supersaturation. Journal of Chemical Physics, 117: 3345-3353.

28 Noppel M., Mirme1 S., Hienola A., Vehkamäki H., Kulmala M. and Wagner P.E. (2007). Reversible Work of the Heterogeneous Formation of an Embryo of a New Phase on a Spherical Charged Conductor Within a Uniform Multicomponent Macroscopic Mother Phase. Nucleation and Atmospheric Aerosols, 327–331.

29 Winkler P.M., Steiner G., Vrtala A., Vehkamäki H., Noppel M., Lehtinen K.E.J., Reischl G.P., Wagner P.E. and Kulmala M. (2008). Heterogeneous Nucleation Experiments Bridging the Scale from Molecular Ion Clusters to Nanoparticles. Science, 319: 1374-1377.

30 Fuchs N. A. (1959). Evaporation and Droplet Growth in Gaseous Media. Pergamon. Oxford.

31 Hinds W.C. (1999). Aerosol Technology. Properties, Behaviour and Measurement of Airborne Particles. Second Edition. John Wiley and Sons, New York. ISBN: 978-0-471-19410-1.

32 Ahn K.H. and Liu B.Y.H. (1990). Particle Activation and Droplet Growth Processes In Condensation Nucleus Counter.-I Theoretical Background. Journal of Aerosol Science, 21:249-261.

33 Baron P.A. and Willeke K. (2001). Aerosol Measurement. Principles, Techniques and Applications. Second Editions. John Willey and Sons. New York.

34 Press W.H., Teukolsky A.A., Vetterling W.T. and Flannery B.P. (2001). Numerical Recipes in Fortran 90. Cambridge University Press.

35 Wiedensohler A. (1988). An Approximation of the Bipolar Charge Distribution for Particles in the Submicron Size Range. Journal of Aerosol Science, 19: 387-389.

36 Allen M.D. and Raabe O.G. (1985). Slip Correction Measurements of Spherical Soild Aerosol Particles in an Improved Millikan Apparatus. Aerosol Science and Technology, 4:269-286.

37 Stolzenburg, M. (1988). An ultrafine aerosol size distribution measuring system. PhD thesis. Department of Mechanical Engineering, University of Minnesota, Minnesota

38 Isella L. and Drossinos Y. (2011).On the Friction Coefficient of Straight-Chain Aggregates. Journal of Colloid and Interface Science, 356: 505-512.

39 Kousaka Y., Endo Y., Ichitsubo H. and Alonso M. (1996). Orientation-Specific Dynamic Shape Factors for Doublets and Triplets of Spheres in the Transition Regime. Aerosol Science and Technology, 24: 36-44.

40 Karlsson M. N. A. and Martinsson B. G. (2003). Methods to Measure and Predict the Transfer Function Size Dependence of Individual DMAs. Journal of Aerosol Science, 34:603-625.

41 Cengel Y. A. and Boles M. A. (2001). Thermodynamics. An Engineering Approach. 4th Edition. McGraw-Hill.

42 Wang X. and Horn H.-G. (2008). Flow Rate Correction for the Model 3790 Engine Exhaust Condensation Particle Counter (EECPC). TSI Application Note EECPC-001.

43 Johnson K. C, Durbin T. D., Jung H., Chaudhary A., Cocker III D. R., Herner J. D., Robertson W. H., Huai T., Ayala A. and Kittelson D. (2009). Evaluation of the European PMP Methodologies during On-Road and Chassis Dynamometer Testing for DPF Equipped Heavy-Duty Diesel Vehicles. Aerosol Science and Technology, 43: 962-969.

44 Mamakos A., Carriero M., Bonnel P., Demircioglu H., Douglas K., Alessandrini S., Forni F., Montigny F., Leseuer D. (2011). EU-PEMS PM Evaluation Program - Second Report - Study on Post DPF PM/PN Emissions. JRC Scientific and Technical Reports, EUR 24793 EN.

45 Rogak, S. and Flagan R. (1992). Bipolar Diffusion Charging of Spheres and Agglomerate Aerosol Particles. Journal of Aerosol Science 23: 693-703.

46 Reischl G., Mäkehä J., Karch R. and Necid J. (1996). Bipolar Charging of Ultrfaine Particles in the Size Range Below 10 nm. Journal of Aerosol Science 27: 931-949.

47 Giechaskiel B., Alessandrini S., Forni F., Carriero M., Krasenbrink A., Spielvogel J., Gerhart C., Wang X., Horn H., Southgate J., Jörgl H., Winkler G., Jing L. and Kasper M. (2008). Calibration of PMP Condensation Particle Number Counters. Effect of Material on Linearity and Counting Efficiency. JRC Scientific and Technical Reports EUR 23495.

European Commission

EUR 25145 EN – Joint Research Centre – Institute for Energy and Transport
Title: Calibration and Modelling of PMP compliant Condensation Particle Counters.
Author(s): Athanasios Mamakos, Giechaskiel Barouch, Yannis Drossinos, Dominique Lesueur, Giorgio Martini, Alois Krasenbrink
Luxembourg: Publications Office of the European Union
2011 – 65 pp. – 21 x 29.7 cm
EUR – Scientific and Technical Research series – ISSN 1831-9424 (online), ISSN 1018-5593 (print)
ISBN 978-92-79-22610-6 (pdf)
ISBN 978-92-79-22609-0 (print)
doi:10.2788/41597

Abstract
The study presents results of calibration experiments for four PMP compliant CPCs (3 TSI's 3790 and a TSI's 3010 operating at lower saturator-condenser temperature differences) tested against a range of calibration particles, including Poly(alpha)-Olefin (PAO), tetracontane (C40), tetradecane (C14) and hexadecane (C16). The experimental data were analyzed using a numerical model developed by Giechaskiel et al. (Journal of Aerosol Science, 42:20-37) which was amended to investigate the effect of line tension, curvature dependence of the surface tension as well as condensational growth of activated particles.
The study also investigated possibilities to verify the linearity of CPCs against an electrometer in the sub 2000 #/cm^3 concentration range. The use of elevated sample flowrates and multiply charged particles of well defined charge status, allowed for some linearity checks down to 300 #/cm^3 concentration levels.

How to obtain EU publications

Our priced publications are available from EU Bookshop (http://bookshop.europa.eu), where you can place an order with the sales agent of your choice.

The Publications Office has a worldwide network of sales agents. You can obtain their contact details by sending a fax to (352) 29 29-42758.

The mission of the JRC is to provide customer-driven scientific and technical support for the conception, development, implementation and monitoring of EU policies. As a service of the European Commission, the JRC functions as a reference centre of science and technology for the Union. Close to the policy-making process, it serves the common interest of the Member States, while being independent of special interests, whether private or national.

LB-NA-25145-EN-N

ISBN 978-92-79-22610-6